Analyzing Dynamical Friction Models with Gravitational Wave Signals of Intermediate Mass Ratio Inspirals

Bachelorarbeit zur Erlangung des akademischen Grades Bachelor of Science in Physik am Institut für Theoretische Physik der Goethe-Universität in Frankfurt am Main

vorgelegt von
Kai Alexander Malik
am
17.03.2025

Erstgutachterin: Prof. Dr. Laura Sagunski
Zweitgutachter: Prof. Dr. Jürgen Schaffner-Bielich

Acronyms

BH	-	Black Hole
CDM	-	Cold Dark Matter
DF	-	Dynamical Friction
DM	-	Dark Matter
DMP	-	Dark Matter Particle
GR	-	General Relativity
GW	-	Gravitational Wave
IMRI	-	Intermediate Mass-Ratio Inspiral
KO	-	Kepler Orbit
MG	-	Modified Gravity
ND	-	Newtonian Dynamics
NG	-	Newtonian Gravity
SIDM	-	Self-Interacting Dark Matter
SR	-	Special Relativity

Contents

1 Introduction

1.1 A brief history of cosmology

Humans have always wondered about the universe and their place in it. The very first pseudosciences tried to find patterns in the stars and planets seen in the night sky and extract truths and information from their behavior. Modern cosmology does basically the same thing, but in a more scientific way, trying to figure out the laws of physics governing our universe that can't be tested here on earth. Gravity in particular is a phenomenon that has only really been understood once its effects on larger scales were observed.

The first model for the universe was a geocentric one, with a stationary earth as the center of the universe and the sun, moon, stars and other planets revolving around it in circles. However, the retrograde motion of planets was already observed early on, contradicting this idea. Sometimes, the planets seem to move in the opposite direction for a few days. Claudius Ptolemy proposed a geocentric model where some planets followed epicycles, explaining their retrograde motion. This model was widely accepted for a very long time.

Around the 1510s to 1530s Nicolas Copernicus pursued a different solution, however he refrained from publishing his results until just before his death in 1543 [1]. He proposed a heliocentric model that placed the sun at the center of the solar system with the earth and other planets orbiting the sun along circles. Although this model was arguably more elegant than the one proposed by Ptolemy, it still was unable to predict the behavior of planets until Johannes Kepler corrected it.

Kepler postulated elliptical orbits instead of circular ones. He formulated two laws of planetary motion in 1609:

1. The orbit of a planet is an ellipse with the Sun at one of the two foci.
2. A line segment joining a planet and the Sun sweeps out equal areas during equal intervals of time.

In 1619 he added a third law:

3. The square of a planet's orbital period is proportional to the cube of the length of the semi-major axis of its orbit.

This model was a lot better at accurately predicting the planetary motion than any of the previous models. An orbit following these laws is called a

Kepler orbit (KO). If the gravitational fields are sufficiently weak and the relative speeds small enough, two massive objects orbit their common center of mass following a KO. If one of the objects has much more mass than the other, as is the case with the sun and planets, that center of mass can be approximated to be at the center of the more massive object. This results in the observed orbital dynamics where the planets seem to orbit a stationary sun.

In a more general approach KOs can be modeled as cone sections [2]. This means they don't necessarily form ellipses or circles, but can also follow a parabolic or hyperbolic trajectory. This will be explored further in subsection 2.2.

Later Isaac Newton laid the foundation of modern physics with his book "Philosophiæ Naturalis Principia Mathematica" (Mathematical Principles of Natural Philosophy) first published in 1687. In there he established a mathematical formulation for the laws of motion and the gravitational interactions between massive objects, called Newtonian dynamics (ND). His model for describing gravity is called Newtonian gravity (NG). With those mathematical tools he was able to derive Kepler's laws of planetary motion, proving its accuracy for systems like our solar system.

However, ND and by extension NG is still incomplete. Firstly ND assumes the possibility of infinite velocity. In ND, if the velocity $\vec{v}_{rel}$ between two reference frames Σ and Σ' as well as the velocity $\vec{v}$ of an object in Σ is known, the velocity $\vec{v'}$ of the same object in Σ' can be calculated simply by adding the two velocity vectors together ($\vec{v'} = \vec{v} + \vec{v}_{rel}$). Also, when accelerating an object with an acceleration $\vec{a}$ for some time t, the change in velocity can be calculated with $\Delta\vec{v} = \vec{a} \cdot t$. Both these facts in theory allow arbitrarily high velocities for any object in any reference frame. Today it is known that the universe actually has a finite speed limit, the speed of light c.

Secondly that speed limit c was observed to be the same in all rest frames, which is also not possible in ND. To account for these phenomena, Einstein introduced his theory of special relativity (SR) in 1905 [3]. At the time he was only concerned with electrodynamics, and SR wasn't able to handle gravity. In order to achieve that, in 1915 he generalized SR, leading to the theory of general relativity (GR). In GR, gravity is not modeled as a force like in NG, but instead arises from the curvature of space-time. This space-time is mathematically described by a 4-dimensional Lorentz-manifold, and its curvature is caused by massive objects, causing it to appear like gravitational

fields generated by these objects.

GR is very successful at describing the orbital mechanics in our solar system, including Mercury's orbit. As mentioned before, the assumption that massive bodies follow a KO is only sufficiently accurate if the gravitational fields are weak enough. Being the closest planet to the sun, the gravitational influence of the sun on Mercury is already too high for that approximation, causing the elliptical orbit to shift over time. While NG can't explain this phenomenon, GR indeed can.

GR also predicted black holes (BHs), gravitational waves (GWs) and gravitational lensing, all of which have since been observed. When considering gravity inside an object with uniform density, the gravitational pull on a test mass towards the center gets weaker the closer to the center it's located. In NG this can be explained by the acting forces, as different volume elements of the massive body pull the test mass in different directions. As the volume that's closer to the center than the test mass scales with r^3 and gravity scales with $1/r^2$, the total force decreases once the test mass moves inside the object. This means gravity is the strongest on the surface of massive objects. BHs are objects with such high densities that nothing can escape their gravitational attraction. To our current knowledge, they are the densest possible objects in the universe.

As the speed limit c includes information itself, it is a reasonable guess that the influence of masses on space-time also propagates with some finite speed. A periodic movement of a massive object also results in a periodic deformation of space-time which propagates as a wave away from the object with that finite speed. Being just the result of the behavior of space-time, these GWs don't require a medium.

In GR light cannot be accelerated and thus always traces a straight line, or geodesic, through space-time. In a curved space-time this means that light should bend according to the curvature, causing light itself to be effected by gravity. This causes gravitational lensing, where light is focused by the space-time curvature caused by great accumulations of masses like galaxies or giant gas clouds. Today gravitational lensing is often used to analyze the content of mass in certain regions.

In short, GR is the most successful theory of gravity to date and can explain a lot of observed phenomena very accurately. Regardless, GR still has its limits. Since the discovery of quantum physics it is clear that GR is incom-

plete as the two theories are incompatible. But even regarding gravity some more modern observations pose a challenge to our existing models including GR.

1.2 The problem with galaxies

While studying different galaxy clusters, Fritz Zwicky in 1933 discovered that the galaxies in the Coma cluster were moving so fast that the mass of visible matter in the cluster wasn't enough to hold the cluster together [4]. He observed the redshift of the galaxies to determine their velocities and used the virial theorem to calculate the total mass needed to hold the cluster together, which was about 400 times larger than the summed-up mass of all the visible matter present in the cluster. At the time this was simply attributed to unseen mass from diffused gas, planets, asteroids etc.

In 1951 Edward Purcell and Harold Ewen discovered the 21 cm hydrogen line [5], making it possible to find cold hydrogen between the stars and galaxies. Around 1962 the first extra-solar X-rays were observed. X-rays are mostly absorbed by the atmosphere which requires detectors like satellite probes outside the atmosphere to pursue X-ray astronomy in a meaningful way. With that hot hydrogen could also be observed. Even with all the hydrogen now being observable, the observed total mass of the Corona cluster was still too small to fit observations.

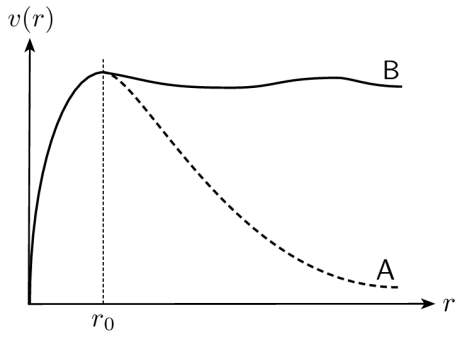

Figure 1: A qualitative sketch of the discrepancy between the expected velocity distribution (A) and the observed distribution (B), taken from [6].

Additionally Vera Rubin ran into the same problem in 1970 when she mapped out the distribution of mass in several galaxies [7]. Similar to the galaxies in the Coma cluster the individual stars in the outer regions of most galaxies were moving way to fast to be held together by the observed mass. Close to the center of the galaxies the measured velocity distribution still matched the expectations relatively well. For higher radii, however, the mass density of the observable matter reduced, which should result in a steep drop in velocity with higher distances from the galaxy's center.

However, the measured velocity distribution curve didn't drop nearly enough, instead it was almost homogeneous for the outer regions of the galaxy.

One possibility to address these observations is to introduce modified gravity (MG). Since GR is not needed to describe galaxies and clusters at large, most MG models start with NG and modify the distance dependency of the gravitational force. The most well-known MG model is modified Newtonian dynamics (MOND) [8], but other approaches exist, some of which also modify GR, like f(R) gravity [9]. As the two models work so well for smaller scales like the solar system, all MG models try to keep NG and GR consistent for these scales, only postulating deviations for high distances. This means MG's effects accumulate for large scale structures, but should never be observed for relatively small systems.

However, there is another, almost trivial way to explain the unusually high velocities. If there has to be more mass than can be seen to explain the rotation curves of galaxies, then perhaps it's just the case that there exists some form of massive matter that simply cannot be seen. This is similar to Zwicky's explanation for the velocity distribution of the Coma cluster. But instead of planets or diffuse gas, which are still composed of baryonic matter, this unseen matter could also be something entirely different that simply doesn't interact electromagnetically. This would explain why, even with the 21 cm hydrogen line and X-ray cosmology, not enough mass was detected.

Even though baryons are particles with an odd number of valence quarks and thus only make up a tiny part of the standard model of particle physics, all matter that's part of the standard model is called baryonic matter. Neutrinos have too little mass and move too fast to be responsible for the unseen mass, and all other baryonic particles are either unstable or interact electromagnetically. Thus the unseen matter has to be non-baryonic and is called dark matter (DM).

The simplest model for DM is cold dark matter (CDM). Cold refers to the fact that its velocity relative to its host galaxy is much smaller than the speed of light. It is also assumed to be collisionless, which means DM particles don't interact with eath other. With the addition of the cosmological constant Λ to explain the expansion of the universe with dark energy, this leads to the ΛCDM model, the currently most widely accepted model of cosmology.

Galaxies containing a cloud of DM, a so-called DM halo, now have the additional mass needed to explain the observed velocities. Almost all galaxies

are expected to have a DM halo [10]. Comparing N-body simulations of CDM with the observed missing masses in galaxies leads to the core-cusp-problem [11]. While the simulations with collisionless DM result in higher halo densities for lower radii, called a "cusp", the rotation curves of galaxies suggest a flat density profile for that region, called a "core". This core can be achieved by assuming self-interacting dark matter (SIDM) [12]. Fig. 2 shows the density profiles for different coupling strength of SIDM compared to the collisionless model.

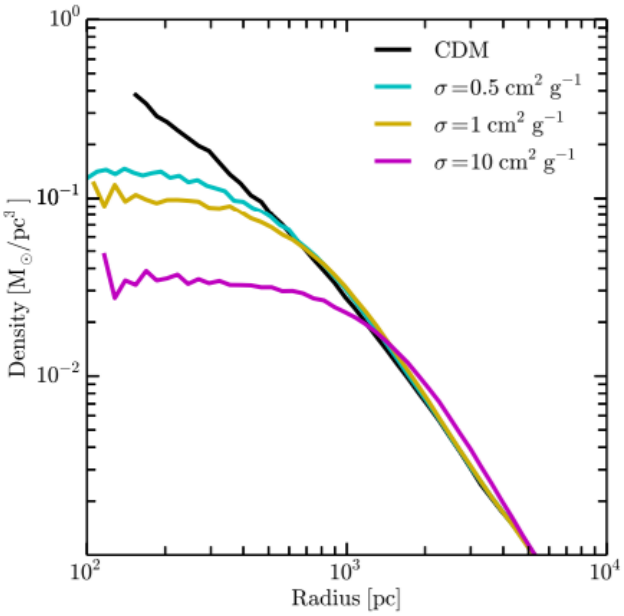

Figure 2: The density profile of a DM halo for different cross sections over unit mass σ, taken from [13].

1.3 Probing dark matter

Since DM does interact neither electromagnetically nor via the strong force, our best bet to find out about its properties is via the gravitational interaction. Since DM is very spread out and the gravitational interaction by far the weakest, this endeavor is not easy. Luckily, BHs can help us out. When a BH slowly accretes dark and baryonic matter and grows adiabatically, it can accumulate a lot of DM into a DM spike of relatively high density. This not only amplifies the observable effects of the DM, but also allows for a clear

distinction between DM effects and effects that could be explained by MG, as MG should not take effect at such low scales.

When a dense object moves through this DM spike, it interacts gravitationally with it. The nature of this interaction offers information about the DM's properties. A prime candidate for such an object could be a second BH. This however poses a problem as BHs cannot be observed directly.

When two very massive objects orbit each other, they periodically curve the space-time around it in different ways, which results in the generation of GWs. Denser objects can get closer to each other, which greatly boosts the strength or amplitude of the GW. This means that the denser the orbiting objects are, the more pronounced is the GW signal produced. This signal contains information about the movement of the bodies relative to each other. Analyzing the GWs emitted from a BH binary thus allows an indirect observation of the BHs.

Additionally, the emission of GWs result in a flux of energy away from the system. This results in a loss of orbital energy, which in turn causes the two objects to get closer to each other over time until they eventually coalescent. This process is called inspiral.

There are three main groups of BHs in our universe that are defined by the order of magnitude of their masses. Stellar BHs have masses comparable to the solar mass, having around $2 - 10^2 M_\odot$. An intermediate mass BH has around $10^4 - 10^5 M_\odot$ and a supermassive BH upwards of $10^6 M_\odot$. A stellar mass object inspiraling into a intermediate mass BH is called intermediate mass ratio inspiral (IMRI). For a supermassive BH it is called extreme mass ratio inspiral (EMRI). This thesis will focus on IMRIs as information sources for DM.

The evolution of the GW signal produced by an IMRI in general only depends on the involved masses and the shape of the initial orbit. However, it can be influenced by both an accretion disk of baryonic matter and a DM spike. Thus analyzing the signal evolution can reveal valuable information about the DM density distribution which in turn can be related to its properties like whether or not DM is actually self-interacting.

In order to detect GWs there already exist some ground-based GW detectors like LIGO [14] or the Virgo interferometer [15]. However for the detection of GWs produced by I/EMRIs, space-based detectors like LISA [16] are needed.

The first gravitational waves were measured in 2015 by the LIGO and Virgo collaboration [17].

This thesis will assume DM particles to exist and gravity to work according to GR for the regarded distances, thus ignoring MG.

2 Theory

In this section all the pieces of our DM probe will be built up step-by-step. Firstly BHs are needed, which will be discussed in subsection 2.1. while the focus of this work is more on the DM and GWs, it is advantageous to first introduce the line element, and BHs offer a great opportunity for that. Next a basic understanding of orbital mechanics is needed. In subsection 2.2 orbits under the assumption of NG are analyzed and the innermost stable circular orbit as well as the escape velocity are introduced. Furthermore, the non-relativistic orbital frequency as a function of distance will be derived. Introduce in subsection 2.3, GWs will act as the signal carriers allowing for the analysis of the binary system. The characteristic strain will be introduced, one of the observables of interest. Once the BH binary with GWs as the signal is set up, the DM can finally be added into the picture, which will be briefly discussed in subsection 2.4. Lastly, it is important to understand how this DM effects our system in order to interpret the information received through the GW signal. For that, in subsection 2.5 the interaction between the DM and the BH binarym is analyzed and the last observables that will be investigated in this thesis are introduced.

2.1 Black holes

In order to approach BHs and later GWs, we need to understand the basics of GR. As mentioned, GR describes space-time as a 4-dimensional manifold. The corresponding metric tensor is denoted by $g_{\mu\nu}$, from which the line element

$$ds^2 = g_{\mu\nu} dx^\mu dx^\nu \tag{1}$$

can be defined. It describes distances on the manifold, which will become important later. Additionally, the metric allows us to analyze the curvature of a manifold. One needs to be careful in doing so, as the choice of a curved coordinate system will also appear as curvature in the metric. To distinguish purely mathematical from physically significant curvature, the Ricci tensor $R_{\mu\nu}$ is defined in [18], from which the Ricci scalar $R = g^{\mu\nu} R_{\mu\nu}$ can be calculated. They are partial derivatives of the metric tensor and contain

information about the nature of its curvature. GR now describes gravity as a consequence of the physical curvature of space-time, which in turn is caused by the energy content of the universe described by the energy-momentum tensor $T_{\mu\nu}$. Solving this for a universe with a homogeneous non-zero energy density everywhere, which is a relatively good approximation for the matter distribution in the universe at very large scales, yields a constant space-time curvature throughout the universe, which means it cannot be static. Since at the time it was still believed that the universe is static, Einstein in [19] introduced the cosmological constant Λ. Today we know that the universe is not static, but instead expanding. However, Λ is still needed to account for the acceleration of that expansion, as seen in [20]. For any given energy distribution $T_{\mu\nu}$, the space-time manifold can then be described by a solution of the Einstein field equations

$$R_{\mu\nu} - \frac{1}{2}Rg_{\mu\nu} + \Lambda g_{\mu\nu} = \frac{8\pi G}{c^4}T_{\mu\nu}. \tag{2}$$

Since G and c are universal constants, we can use geometrized units where $G = c = 1$.[1] Additionally, for this work's purposes Λ can be neglected. This simplifies the field equations to

$$R_{\mu\nu} - \frac{1}{2}Rg_{\mu\nu} = 8\pi T_{\mu\nu}. \tag{3}$$

This is now a set of 16 equations, one for each possible configuration of $\mu, \nu \in \{0, 1, 2, 3\}$. However, all the involved tensors are symmetric, which reduces (3) to 10 independent equations. Since $R_{\mu\nu}$ and R are partial derivatives of $g_{\mu\nu}$, the field equations themselves are a set of partial differential equations for a given $T_{\mu\nu}$. Thus, if the energy content of the universe and its flux is known, one could in theory solve for the corresponding metric tensor and thus find the line element. However since this requires solving 10 independent non-linear differential equations, in practice this is unfeasible.

Two trivial solutions can be found for vacuum where $T_{\mu\nu} = 0$. These solutions are

$$g_{\mu\nu} = \begin{pmatrix} -1 & 0 & 0 & 0 \\ 0 & 1 & 0 & 0 \\ 0 & 0 & 1 & 0 \\ 0 & 0 & 0 & 1 \end{pmatrix} \quad \text{and} \quad g_{\mu\nu} = \begin{pmatrix} 1 & 0 & 0 & 0 \\ 0 & -1 & 0 & 0 \\ 0 & 0 & -1 & 0 \\ 0 & 0 & 0 & -1 \end{pmatrix} \tag{4}$$

[1] Note that geometrized units will be used for the remainder of this thesis, which impacts not only the Einstein field equations, but other equations and values of observables as well.

with the corresponding line elements

$$ds^2 = -dt^2 + dx^2 + dy^2 + dz^2 \quad \text{and} \quad ds^2 = dt^2 - dx^2 - dy^2 - dz^2. \tag{5}$$

The two solutions are physically equivalent, and both lead to special relativity. This solution duality exists for all solutions of the field equations, and it's up to convention which one to use. For further explanation I will use the first solution where the time component is negative.

Aside from this trivial one, Einstein himself didn't yet find another solution when he published his theory. Instead, it was Karl Schwarzschild who discovered the first non-trivial solution in 1916 [21]. He assumed spherical symmetry and used spherical coordinates for space, which lead to the Schwarzschild metric

$$g_{\mu\nu} = \begin{pmatrix} -\left(1 - \frac{r_S}{r}\right) & 0 & 0 & 0 \\ 0 & \frac{1}{\left(1 - \frac{r_S}{r}\right)} & 0 & 0 \\ 0 & 0 & r^2 & 0 \\ 0 & 0 & 0 & r^2 \sin^2\theta \end{pmatrix} \tag{6}$$

with corresponding line element

$$ds^2 = -\left(1 - \frac{r_S}{r}\right) dt^2 + \frac{1}{(1 - \frac{r_S}{r})} dr^2 + r^2 d\theta^2 + r^2 sin^2\theta d\varphi^2 \tag{7}$$

where r_S is a free parameter and called the Schwarzschild radius. One can immediately see that this equation has two singularities, one with spatial dimension 0 at $r = 0$ and one with spatial dimension 2 at $r = r_S$. The physical curvature of the manifold depends on r_S and is generally non-zero, which means there has to be some energy or mass, which is assumed to be concentrated in the first singularity. This first singularity is a physical one, which means it will be present in all coordinate systems. The second singularity on the other hand is a mathematical one and can be removed with the appropriate coordinate system. However, this singularity sill has physical significance which becomes clear when we look at the regime $r < r_S$. Here, $(1 - \frac{r_S}{r})$ becomes negative, which means the signs of dt^2 and dr^2 in eq. (7) flip:

$$ds^2 = \kappa dt^2 - \frac{1}{\kappa} dr^2 + r^2 d\theta^2 + r^2 sin^2\theta d\varphi^2 \tag{8}$$

where $\kappa = -(1 - \frac{r_S}{r})$ is positive. This means all time-like distances now have to involve a change in r, and in turn all paths where r doesn't change (enough) are space-like. This means in this regime the future light cone

is rotated towards negative r and thus towards the physical singularity in the center, and all paths inevitably end up there [22]. This includes the path of light itself, so not even light or other kinds of radiation can escape this regime, which is why objects which fulfill the Schwarzschild solution are called "black holes". Since the second (mathematical) singularity cuts off all events inside this regime from the outside, it is also referred to as the event horizon of the BH.

In general, BHs can have charge, momentum, angular momentum and energy. The energy can be expressed as mass through the mass-energy equivalence $E = mc^2$ and which is concentrated in the central singularity. Since the energy content and thus the mass of the BH dictate the curvature of space-time around it and the same curvature in eq. (7) is solely described by r_S, we can relate the mass and the Schwarzschild radius with $r_S = 2m$[2]. Eq. (7) only describes static, non-rotating and uncharged BHs. To get a moving BH and thus momentum, one can simply boost the system. It should be intuitively obvious that a moving BH behaves in the same way as a stationary one. For a BH with Schwarzschild radius r_S and angular momentum L we need the Kerr metric [23], which leads to the line element

$$\begin{aligned} ds^2 = &- \left(1 - \frac{r_S r}{\Sigma}\right) dt^2 + \frac{\Sigma}{\Delta} dr^2 + \Sigma d\theta^2 \\ &+ \left(r^2 + \left(\frac{2L}{r_S}\right)^2 + \frac{r_S r a^2}{\Sigma} sin^2\theta\right) sin^2\theta d\varphi^2 - \frac{4rLsin^2\theta}{\Sigma} dt d\varphi \end{aligned} \tag{9}$$

where $\Sigma = r^2 + \left(\frac{2L}{r_S}\right)^2 \cos^2\theta$ and $\Delta = r^2 - r_s r + \left(\frac{2L}{r_S}\right)^2$. For a charged BH the Reissner–Nordström metric [24] and for a rotating and charged BH the Kerr–Newman metric [25] is needed, both of which won't be discussed as all considered BHs can be assumed to have negligible charge.

2.2 Kepler orbits

Now that we have the first component for our DM probe, we want to take two BHs and let them orbit each other. Even at quite some distance away from the event horizon of a BH, the space-time curvature is still so large that NG breaks down pretty drastically. Nevertheless, KOs can be useful as we can look at the masses and momenta of the binary system at any given time, look at what KO they would follow in NG and then analyze

[2]Mind the use of geometrized units. To get from geometrized units to SI units, take $r_S^{[SI]} = (G/c^2) r_S^{[gu]}$

the change of that hypothetical orbit during the inspiral. As mentioned, KOs take the form of cone sections, which can be circles, ellipses, parabolas or hyperbolas. Ellipses are a good starting point for a generalized description of KOs, as they can easily transition into circles and parabolas.

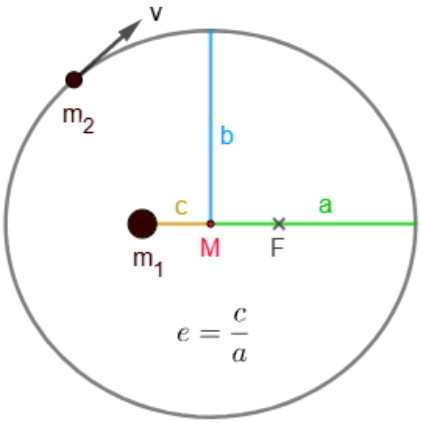

Figure 3: A sketch of an elliptical orbit with the focal points being F and the position of the primary of mass m_1, the semi-major axis a, semi-minor axis b and linear eccentricity c.

Figure 3 shows a simple visualization of a primary object of mass m_1 (in the following just called primary) that is orbited by a secondary object of mass m_2 (in the following just called secondary). To be more precise, the two objects orbit each other, so they will both follow a KO around their shared center of mass. If we have $m_2 \ll m_1$, which is the case for an IMRI, we can however approximate the center of mass to be at the position of the primary and the primary itself to be stationary. The trajectory of the secondary then forms an ellipse with one of its focal points being the primary. The other one is some point F in space. The midpoint M can be defined between F and the primary. The semi-major axis a is the maximal, the semi-minor axis b the minimal distance from M to the ellipse. The distance from M to either one of the foci is called the linear eccentricity c, from which the eccentricity $e = \frac{c}{a}$ can be defined. While the linear eccentricity c depends on the shape and size of the ellipse, the eccentricity e only depends on the shape. Since both a and c are defined positive for circles and ellipses and negative for hyperbolas, e can only ever be positive. $e = 0$ means that the foci have no distance and both lie in point M, which describes a circle with radius $r = a = b$. The cases $0 < e < 1$ describe ellipses of different shapes. The larger the eccentricity gets, the less circular the orbit becomes, and the closer the foci and the ellipse get compared to a. In the extreme case of $e = 1$, this results in either a straight line where $b = 0$ or an infinite distance between the foci where $a = \infty$. The second case describes a parabola.

Now e can also be greater than 1, which describes hyperbolic trajectories, which will become relevant later in subsection 2.5. These trajectories are

running between M and one of the foci, are curved toward the focus and asymptotically approach a straight line along which they run towards infinity. This means all orbits with $e \geq 1$ eventually reach infinity, don't close in on themselves and are thus called open orbits. Orbits with $e < 1$ on the other hand are called closed orbits. Since there exists a maximal distance for the two objects in a closed orbit, they can be said to be bound together, so that closed orbits are also called bound orbits. Conversely, open orbits are also called unbound orbits.

Since NG is a classical theory, we can define a gravitational potential similar to the electric potential in electrodynamics and thus easily find the potential energy due to gravity

$$U = -\frac{m_1 m_2}{r}, \tag{10}$$

where r is the distance between primary and secondary. If we use the approximation from earlier and define the primary to be static, the total energy of the binary system is given by the potential energy and the kinetic energy

$$K = \frac{m_2 v^2}{2} \tag{11}$$

of the secondary. The total energy of an orbit is thus given by $E = K + U$. In a circular orbit the gravitational or centripetal force towards the primary must be just as strong as the fictional centrifugal force away from the primary. This condition gives us

$$\begin{aligned} K &= \frac{m_1 m_2}{2r} \\ E = K + U &= \frac{m_1 m_2}{2r} - \frac{m_1 m_2}{r} = -\frac{m_1 m_2}{2r}, \end{aligned} \tag{12}$$

which can be generalized for elliptical orbits [26] to

$$E = -\frac{m_1 m_2}{2a}. \tag{13}$$

Furthermore, for any given r we can calculate the exact velocity v_{circ} required to form a circular orbit[3], as

$$\begin{aligned} \frac{m_2 v_{circ}^2}{2} &= \frac{m_1 m_2}{2r} \\ v_{circ}(r) &= \sqrt{\frac{m_1}{r}}. \end{aligned} \tag{14}$$

[3]Note that for a circular orbit the direction of the velocity is also important and needs to be perpendicular to a straight line connecting the two objects, which does not become apparent from eq. (14).

E is equivalent to the kinetic energy the secondary would have at an infinite distance away from the primary. Since for an ellipse this energy is negative as all values in (13) are positive, the absolute value of E is the energy that's required to be put into the system so that the secondary could theoretically reach infinity with zero velocity. Then this case of $E = 0$ is the energy of an parabolic orbit. At any distance, for such an orbit the kinetic and absolute value of the potential energy are the same, so

$$\begin{aligned} K &= U \\ \frac{m_2 v_{esc}^2}{2} &= \frac{m_1 m_2}{r} \\ v_{esc}(r) &= \sqrt{\frac{2m_1}{r}}, \end{aligned} \tag{15}$$

where v_{esc} is called the escape velocity of m_1 at the distance r. Sitting at a distance r away from the primary, $v_{esc}(r)$ is the minimal velocity that the secondary needs to eventually get arbitrarily far away from the primary. Comparing this to eq. (14), we can see that this velocity is exactly $\sqrt{2}$ times the velocity needed to form a circular orbit at the same distance.

If we define a to be negative for hyperbolic orbits, this formula even holds for those orbits; in this case E is positive and equal to the kinetic energy at an infinite distance. However, once the secondary has reached a distance r_{inf} where $K \gg U$, the velocity won't change much any more and we can approximate $v_{inf} \approx v_\infty$. The relative velocity of a secondary outside a sphere of radius r_{inf} around the primary can thus simply be used to calculate the total orbital energy. Together with the direction of the velocity vector compared to the position of the primary, the energy will dictate the shape of the hyperbolic trajectory if the two objects gravitationally interact. If the secondary stays outside this sphere, the interaction between the two objects can be neglected; in such a case one could say the primary didn't influence the secondary at all. r_{inf} is thus called the radius of influence and the corresponding sphere around the primary the sphere of influence of the primary.

Of course the choice of r_{inf} is to some extent arbitrary and up to definition. This definition is adapted to a considered problem, depending on how accurate the approximation of neglecting the interaction is. If there are other objects around, like stars in a galaxy, the interaction between the secondary and the stars can at some point dominate the interaction with the primary. If we don't have a well-defined star distribution, all the gravitational interactions can be seen as some sort of random noise, in which the comparably

small interaction with the primary drowns.

Going to the other extreme of placing the objects very close to each other, we eventually reach the point where the space-time curvature gets so extreme that no stable circular orbits are possible any more. The closest stable circular orbit at distance r_{isco} is called the innermost stable circular orbit and given by [27]

$$\begin{aligned} r_{isco} &= m_1 \left(3 + Z_2 \pm \sqrt{(3 - Z_1)\,(3 + Z_1 + 2Z_2)}\right) \\ Z_1 &= 1 + \sqrt[3]{1 - \left(\frac{a}{m_1}\right)^2} \left(\sqrt[3]{1 + \left(\frac{a}{m_1}\right)} + \sqrt[3]{1 - \left(\frac{a}{m_1}\right)}\right) \\ Z_2 &= \sqrt{3\left(\frac{a}{m_1}\right)^2 + Z_1^2}, \end{aligned} \tag{16}$$

where a in this case is the angular momentum per unit mass. For a non-rotating BH where $a = 0$ this simplifies to

$$r_{isco} = 6m_1 = 3r_S. \tag{17}$$

In this thesis I will ignore the regime of less distance to the primary than the innermost stable orbit, so everything relevant will happen in the regime $r_{isco} < r < r_{inf}$.

Since for a closed orbit the secondary travels through the same points periodically, we can look at the time T between two instances in which it has the exact same position. For a circular orbit this is easy to do as speed and distance don't change throughout the orbit, and we have

$$\begin{aligned} v_{circ}(r) &= \sqrt{\frac{m_1}{r}} = \frac{2\pi r}{T} \\ T(r) &= \frac{2\pi r\sqrt{r}}{\sqrt{m_1}} = \frac{2\pi}{\sqrt{m_1}} r^{\frac{3}{2}}. \end{aligned} \tag{18}$$

From that the mean orbital frequency $\mathcal{F}$ and mean circular frequency ω

$$\begin{aligned} \mathcal{F}(r) &= T^{-1}(r) = \frac{\sqrt{m_1}}{2\pi} r^{-\frac{3}{2}} \\ \omega(r) &= 2\pi\mathcal{F}(r) = \sqrt{m_1} r^{-\frac{3}{2}} \end{aligned} \tag{19}$$

of the orbit can be calculated. Once again, the same equations can be used for elliptical orbits if we replace r with the more semi-major axis a, as seen

in [28]. For completion I want to mention that for a general case where both objects actually orbit the common center of mass, the total mass $m = m_1+m_2$ has to be used. Since the mass ratio is pretty large if we compare the BHs of an IMRI or the mass of a DM particle to the solar mass, in both cases our approximation from before is accurately enough. Using the total mass and an elliptical orbit however yields the most general expression for the mean orbital frequencies of closed orbits:

$$\begin{aligned} \mathcal{F}(a) &= \frac{\sqrt{m}}{2\pi} a^{-\frac{3}{2}} \\ \omega(a) &= \sqrt{m} a^{-\frac{3}{2}}. \end{aligned} \tag{20}$$

2.3 Gravitational waves

Now that we have a BH binary system and understand how they orbit each other under the assumption of NG, we want to actually receive information from them. As mentioned, a good way to do that is through GWs which we will now examine more closely. This deviation doesn't follow any specific literature but is instead put together using all the referenced sources. To approach GWs, we need to go back to GR and the metric tensor $g_{\mu\nu}$. We can always find oscillating solutions for the Einstein field equations in various circumstances, e.g. simply with an oscillating energy-momentum tensor. What we're interested in however are propagating GWs, so they should also exist in vacuum. To approach that we can start with the metric tensor for special relativity, the Minkowski metric $\eta_{\mu\nu}$ and apply a small perturbation $h_{\mu\nu} \ll 1$:

$$\begin{aligned} g_{\mu\nu} &= \eta_{\mu\nu} + h_{\mu\nu} \\ ds^2 &= (\eta_{\mu\nu} + h_{\mu\nu}) x^{\mu} x^{nu}. \end{aligned} \tag{21}$$

To make things more compact we can calculate the trace reversed $\overline{h}_{\mu\nu}$ of $h_{\mu\nu}$ with

$$\overline{h}_{\mu\nu} = h_{\mu\nu} - \frac{1}{2} \eta_{\mu\nu} h^{\sigma}{}_{\sigma}. \tag{22}$$

Now since we want something wave-like it is a good guess to let $\overline{h}_{\mu\nu}$ be some amplitude tensor $A_{\mu\nu}$ multiplied by a wave equation

$$\overline{h}_{\mu\nu} = A_{\mu\nu} \cos(k_{\sigma} x^{\sigma}) \tag{23}$$

where $k_{\sigma} = (-\omega, k_x, k_y, k_z)$ is the wave vector of the GW. Now we can make some guesses and check if they are compatible with eq. (3), which, since we are in vacuum, demands that the Ricci tensor vanishes. That means not

every configuration of $A_{\mu\nu}$ is possible. If we set $A_{11} = 1$ and all other components to 0 for example, not all components of $R_{\mu\nu}$ vanish, which shows $\overline{h}_{\mu\nu}$ cannot only oscillate in the x-direction alone. Since the choice of coordinates is arbitrary this means $\overline{h}_{\mu\nu}$ cannot only oscillate in any direction alone in general. Another guess would be to combine two different directions of oscillation, which for a wave moving in the z-direction could be the x- and y-directions. That leads to

$$A_{\mu\nu} = \begin{pmatrix} 0 & 0 & 0 & 0 \\ 0 & \alpha & 0 & 0 \\ 0 & 0 & \alpha & 0 \\ 0 & 0 & 0 & 0 \end{pmatrix} \text{ or } A_{\mu\nu} = \begin{pmatrix} 0 & 0 & 0 & 0 \\ 0 & \alpha & 0 & 0 \\ 0 & 0 & -\alpha & 0 \\ 0 & 0 & 0 & 0 \end{pmatrix}. \tag{24}$$

For the first result the Ricci tensor also doesn't vanish, however it does for the second one. Using the second result and rotating the frame of reference around the z-axis yields

$$A_{\mu\nu} = \begin{pmatrix} 0 & 0 & 0 & 0 \\ 0 & 0 & \alpha & 0 \\ 0 & \alpha & 0 & 0 \\ 0 & 0 & 0 & 0 \end{pmatrix} \tag{25}$$

as another possibility.

Before we continue, we should check if there are any more independent degrees of freedom for a GW. We already know that $g_{\mu\nu}$ is symmetric, which immediately reduces the possible degrees of freedom from 16 to 10. To further decrease them we can make use of the right gauge conditions. First we can apply the Lorentz gauge which demands

$$\partial_\nu \overline{h}^{\mu\nu} = 0, \tag{26}$$

giving 4 additional constrains as we have 4 independent equations, one for each $\mu \in \{0, ..., 3\}$. The Lorentz gauge is a group of different coordinate systems, so we can narrow it down even more by choosing the appropriate subset of the Lorentz group. Secondly we can choose a coordinate system where the components of $A_{\mu\nu}$ are orthogonal to an observers four-velocity U^μ, so we get the constraint

$$U^\mu A_{\mu\nu} = 0. \tag{27}$$

As the wave amplitude is now orthogonal to U^μ and the GW can thus be seen as a transverse wave, the gauge is called transverse gauge. This appears

to also give 4 constraints, which is correct, but only 3 of them are new independent constrains. If we go into the rest frame of the observer where only the time component of U^μ is non-zero, eq. (27) requires $A_{0\mu}$ to be zero for all μ, which in matrix notation would leave a 3 by 4 block of non-zero components, leaving only 3 meaningful equations for eq. (26), so it produces only 3 new constraints. This means that from the remaining 6 independent components still 3 remain. We can get one last constraint by making $A_{\mu\nu}$ traceless, which means

$$A^\mu{}_\mu = 0. \tag{28}$$

This makes one component of the main diagonal of the tensor dependent on the other three, reducing the amount of independent components to 2. Since in the gauge our wave is now transverse and $A_{\mu\nu}$ traceless, this gauge is called transverse-traceless (TT)-gauge.

As $A_{\mu\nu}$ is constant, the derivative in $\partial_\nu \overline{h}^{\mu\nu}$ only applies to the cosine, which gives

$$\partial_\nu \overline{h}^{\mu\nu} = A^{\mu\nu} k_\nu \sin(k_\sigma x^\sigma) \tag{29}$$

which in the Lorentz gauge (26) has to be zero, which implies

$$A^{\mu\nu} k_\nu = A_{\mu\nu} k^\nu = 0. \tag{30}$$

Using the TT-gauge we can now stay in the rest frame of U^μ and analyze a GW traveling in the z-direction. We then have $k_\mu = (-\omega, 0, 0, k_z)$ and $U^\mu = (U^t, 0, 0, 0)^T$ which together with eq. (30) and eq. (27) reduces $A_{\mu\nu}$ to

$$A_{\mu\nu} = \begin{pmatrix} 0 & 0 & 0 & 0 \\ 0 & \alpha & \beta & 0 \\ 0 & \gamma & \delta & 0 \\ 0 & 0 & 0 & 0 \end{pmatrix}. \tag{31}$$

The tensor symmetry demands $\beta = \gamma$, and eq. (28) demands $\alpha + \delta = 0$, so

$$A_{\mu\nu} = \begin{pmatrix} 0 & 0 & 0 & 0 \\ 0 & \alpha & \beta & 0 \\ 0 & \beta & -\alpha & 0 \\ 0 & 0 & 0 & 0 \end{pmatrix} \tag{32}$$

which is very similar to eqs. (24) and (25) which we know to be solutions that are independent from each other. This means we can split $A_{\mu\nu}$ into a sum of two tensors that are also solutions to the field equations themselves.

2.3.1 Impact on the line element

We then have two different line elements

$$\begin{aligned} ds_\alpha^2 &= -dt^2 + (1+A)dx^2 + (1-A)dy^2 + dz^2 \\ ds_\beta^2 &= -dt^2 + dx^2 + dy^2 + dz^2 + 2B\,dxdy \\ A &= \alpha\,\cos(-\omega t + k_z z + \varphi_{0,\alpha}) \\ B &= \beta\,\cos(-\omega t + k_z z + \varphi_{0,\beta}). \end{aligned} \tag{33}$$

As time is not curved here, we can just use it as a parameter like in classical physics and concentrate on the spacial coordinates. Now let O be the origin of our spacial coordinate system and consider a point P in the $x-y$-plane with spacial coordinates $(x_P, y_P, 0)$. The distance $s_\alpha = \int ds_\alpha$ between O and P is then given by

$$s_\alpha^2 = (1+A)x_P^2 + (1-A)y_P^2 \tag{34}$$

which can be split up into two separate distances, one for each direction:

$$\begin{aligned} s_{\alpha,x} &= \sqrt{1+A}x_P \\ s_{\alpha,y} &= \sqrt{1-A}y_P \\ s_\alpha^2 &= s_{\alpha,x}^2 + s_{\alpha,y}^2. \end{aligned} \tag{35}$$

$s_{\alpha,x}$ then describes the distance of P to the y-axis and $s_{\alpha,y}$ the distance to the x-axis. When A now oscillates, both distances change opposite to each other, so whenever $s_{\alpha,x}$ increases, $s_{\alpha,y}$ decreases and vice versa. For any given A these distances can be compared to the distances $s_{\alpha,x,0}$ and $s_{\alpha,y,0}$ in the case $A = 0$, and a displacement vector $\vec{D}_{P,\alpha}$ for P can be defined as

$$\vec{D}_{P,\alpha} = \begin{pmatrix} s_{\alpha,x} - s_{\alpha,x,0} \\ s_{\alpha,y} - s_{\alpha,y,0} \\ 0 \end{pmatrix} = \begin{pmatrix} (\sqrt{1+A} - 1)x_P \\ (\sqrt{1-A} - 1)y_P \\ 0 \end{pmatrix}. \tag{36}$$

Taylor expanding this as a function of A yields

$$\vec{D}_{P,\alpha} = \left(\frac{A}{2} + \mathcal{O}\left(A^2\right)\right) \begin{pmatrix} x_P \\ -y_P \\ 0 \end{pmatrix} \tag{37}$$

where $\mathcal{O}(A^2)$ can be neglected since

$$h_{\mu\nu} \ll 1 \implies A_{\mu\nu} \ll 1 \implies \alpha \ll 1 \implies A \ll 1.$$

That means P stays in the $x-y$-plane but is periodically shifted by $\vec{D}_{P,\alpha}$ when the GW passes. Doing all that for $ds_\beta = \int ds_\beta$ as well seems a little

more difficult because of the mixed $dxdy$ term. Remember however that we got from eq. (24) to (25) through a simple rotation around the z-axis, namely a 90° right-handed rotation. Applying the same rotation to the displacement vector and transforming A into B yields

$$\vec{D}_{P,\beta} = \left(\frac{B}{2} + \mathcal{O}\left(B^2\right)\right) \begin{pmatrix} y_P \\ x_P \\ 0 \end{pmatrix}, \tag{38}$$

where $\mathcal{O}(B^2)$ can once again be neglected. The two solutions are independent from each other and can stack, so the total displacement P experiences is given by $\vec{D}_P = \vec{D}_{P,\alpha} + \vec{D}_{P,\beta}$. Since the selection of P was arbitrary the displacement vectors can be expanded to displacement fields

$$\begin{aligned} \vec{D}_\alpha(x, y, A) &\approx \frac{A}{2} \begin{pmatrix} x \\ -y \\ 0 \end{pmatrix} \\ \vec{D}_\beta(x, y, B) &\approx \frac{B}{2} \begin{pmatrix} y \\ x \\ 0 \end{pmatrix} \\ \vec{D}(x, y, A, B) &\approx \frac{A}{2} \begin{pmatrix} x \\ -y \\ 0 \end{pmatrix} + \frac{B}{2} \begin{pmatrix} y \\ x \\ 0 \end{pmatrix}. \end{aligned} \tag{39}$$

The two different displacement effects can now be seen as the polarizations of the GW. Since $\vec{D}_\alpha(x, y, A)$ stretches and compresses the distances along a plus-shaped field, it is called the plus-polarization (+-polarization), while $\vec{D}_\beta(x, y, B)$ stretches and compresses it along a cross-shaped field and is thus called the cross-polarization (×-polarization). Figure 4 shows the displacement field for each of the polarizations around O. It's important to keep in Mind that $\vec{D}_\alpha(x, y, A)$ and $\vec{D}_\beta(x, y, B)$ are proportional to A and B which in turn oscillate, which means the displacement itself and thus also the point P oscillate.

Considering the discovery of the two polarizations the notation can be changed accordingly:

$$\alpha \to h_+;\ \beta \to h_\times$$

$$s_\alpha \to s_+;\ s_\beta \to s_\times$$

$$\varphi_{0,\alpha} \to \varphi_{0,+};\ \varphi_{0,\beta} \to \varphi_{0,\times}$$

$$D_\alpha \to D_+;\ D_\beta \to D_\times.$$

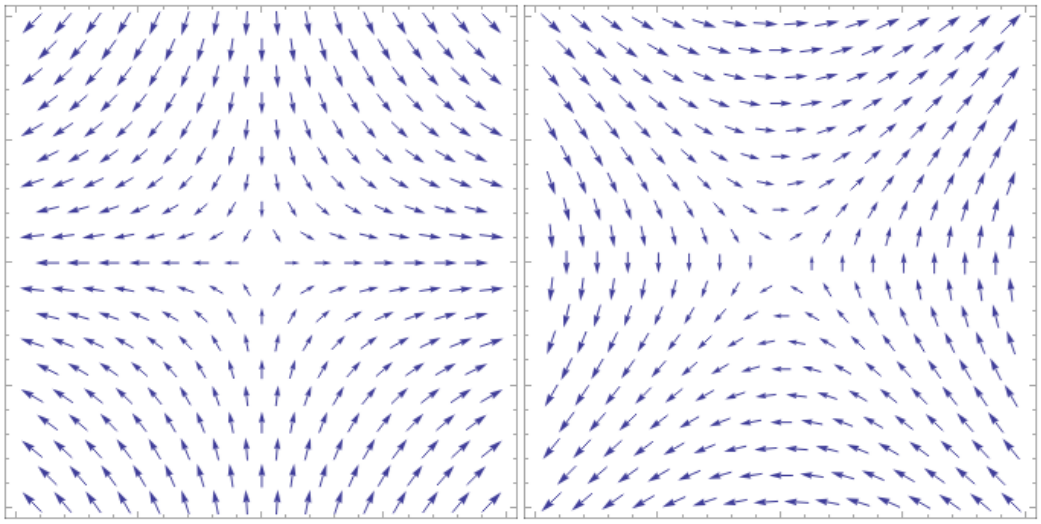

Figure 4: A graphical representation of the displacement vector fields $\vec{D}_\alpha(x,y)$ (on the left) and $\vec{D}_\beta(x,y)$ (on the right) around the origin O for some given values A and B, created with WolframAlpha. The x-axis is horizontal and points to the right and the y-axis is vertical and points upwards.

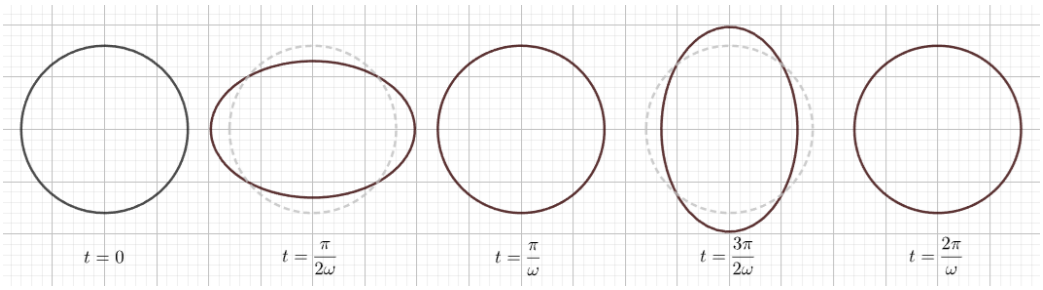

Figure 5: The exaggerated effects of a +-polarized GW traveling in the z-direction on a ring in the $x-y$-plane in the TT-gauge, created with GeoGebra. Here $\varphi_{0,+} = -\frac{\pi}{2}$, with the x-axis being horizontal and pointing to the right and the y-axis being vertical and pointing upwards.

Let's now consider a collection of points around O in the $x-y$-plane where x^2+y^2 is the same constant value for every point. For $A = B = 0$ this forms a circle around O. A GW now causes all the points to oscillate according to eq. (39), which is depicted in fig. 5 for +-polarization.

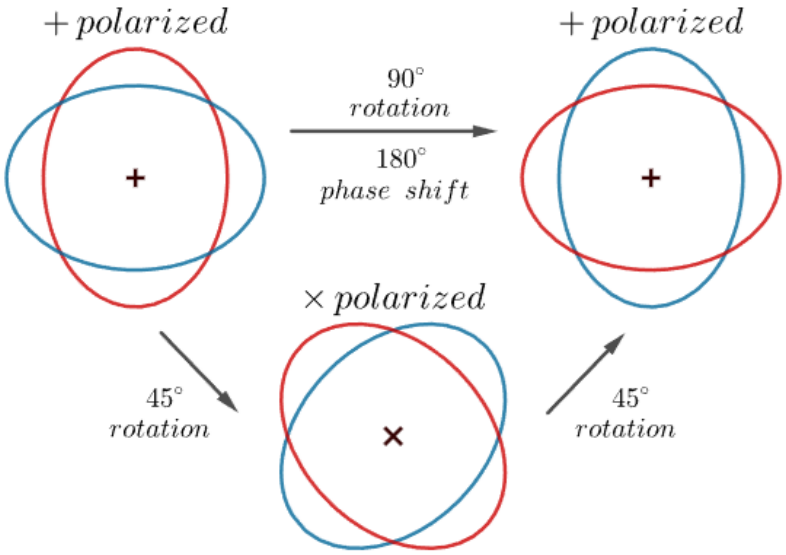

Figure 6: Visual representation of the transformation of the polarizations with rotation around the z-axis, created with GeoGebra. The two extreme cases of the deformation of a circle around the z-axis are shown to represent the effect of the GW on the line element. The x-axis is horizontal and points to the right and the y-axis is vertical and points upwards.

The +-polarization was turned into a ×-polarization using a 90° rotation of the individual displacement vectors. When looking closely at fig. 4 however, it becomes apparent that due to the field's symmetry one can also switch between the polarizations by rotating the entire field by 45°. Rotating it by 90° results in the same polarization, but with the arrows flipped, which corresponds to a 180° phase shift. This can also be seen in fig. 6. This is similar to the x- and y-polarizations of electromagnetic waves. There, a 180° rotation of the entire wave around its direction of propagation results in the same polarization, but with the field vectors flipped. It takes a full 360° rotation to completely return to the starting state, which can be related to the photon's spin of 1. The spin determines how often a particle returns to its exact initial state during a 360° rotation. Since the GW returns to its

initial state after only a 180° rotation with no phase shift, it acts similarly to something with spin-2[4].

Also, similar to light the two polarizations are completely independent from each other. A relative phase shift of either 0° or 180° between the polarizations results in a linearly polarized GW, which causes a periodic compression and stretching of the circle in one direction similar to the pure polarizations. Other relative phase shifts, where A and B are both non-zero, on the other hand describe elliptically polarized GWs. The special cases where $A = B$ and the relative phase shift is either 90° or 270° describes a circularly polarized GW.

2.3.2 Impact on matter and the BH binary

Now that it's clear how coordinate points are effected by GWs, the question remains what the interaction with matter looks like. Placing test particles along the previously defined circle doesn't immediately show that effect, as so far only the oscillation of the coordinate system itself was considered. If the particles also gain coordinate velocity from the GW, this could counteract the coordinate oscillation and result in the particles not actually moving, rendering GWs to be just a mathematical artifact. To analyze this for a $+$-polarized GW the changes of rate of the coordinate velocities u_μ were calculated using Maxima[5]:

$$\begin{aligned} \frac{du_x}{dt} &= u_x(u_t - u_z)\frac{dA}{dt} \\ \frac{du_y}{dt} &= -u_y(u_t - u_z)\frac{dA}{dt}. \end{aligned} \tag{40}$$

It can be seen that, if the particles have no coordinate velocity in the $x-y$-plane at any point, then their coordinate acceleration in the same plane is also 0, even under the influence of a GW moving in the z-direction, thus the coordinate velocity will stay 0 indefinitely. This means the ring of test particles will move along with the deformation of the coordinate system; GWs can impact matter. This is great news as this means it is indeed possible to detect GWs and thus analyze the behavior of the BH binary. This also means that GWs carry energy.

[4]If the graviton exists, as a carrier particle it should have integer spin. However, it should neither be Higgs-like nor photon-like, so neither have spin-0 nor spin-1, with the next-simplest case being a spin-2 graviton.

[5]`https://maxima.sourceforge.io`

As the two BHs orbit each other, they emit GWs with the frequency $f = \omega_{GW}/2\pi$ being a harmonic of the orbital frequency $\mathcal{F}$ with

$$f^{(n)} = n\mathcal{F} \tag{41}$$

for the n-th harmonic. Thus when analyzing the frequency of the GW, the evolution of the orbital frequency of the binary can be deduced, from which a lot can be learned about the system. The GWs produced by the BH binary are not perfect spherical waves, but they still radiate in all directions away from the binary. This means that similar to a spherical wave the energy density and thus also the amplitude or "strength" of the wave is inversely proportional to the square of the distance from the binary. So all the GWs we will receive near earth from such binaries are relatively weak which conforms with the definition of the perturbation $h_{\mu\nu}$ of the metric being very small. This also means that the effects these GWs have on matter here are tiny, which makes them very hard to detect. To analyze the detectability of the GW signal, the characteristic strain can be defined as [29]

$$h_c(f)^2 = 4f^2|\tilde{h}(f)|^2 \tag{42}$$

where $\tilde{h}(f)$ is the Fourier transform of the GW signal. To analyze the detectability of a signal with a given characteristic strain with a given detector, h_c can be compared to the noise amplitude

$$h_n(f)^2 = fS_n(f) \tag{43}$$

of the detector. $S_n(f)$ is a function specific to the detector under consideration that yields the strength of the background noise of a given frequency in the detector, e.g. caused by random fluctuations. With h_c and h_n the signal to noise ratio can be calculated with [29]

$$\varrho^2 = \int_\infty^\infty d\ \ln(f) \left|\frac{h_c(f)}{h_n(f)}\right|^2 . \tag{44}$$

Not all GW detectors can detect all kinds of frequencies. Earth-based detectors like LIGO and VIRGO have a frequency range of around $10 - 10^4$Hz [29]. IMRIs however emit GWs primarily below 10Hz [30]. To make them detectable as well, LISA and eLISA are needed, which can theoretically detect signals with a frequency of around $10^{-5} - 1$Hz [29]. Realistically however, as we will see later when comparing h_c of an IMRI with h_n of LISA, the detector might only pick up the signal at around $10^{-4} - 10^{-2}$Hz. The frequency evolution of the signal in this range can still give valuable information about the system and, by extension, about the DM.

It is often unpractical or sometimes even impossible to observe an inspiral in its entirety. However, a lot of information can also be gained from looking at the evolution of the orbital frequency. With that evolution the braking index n_b can be defined as [31]

$$n_b = \frac{\mathcal{F}\ddot{\mathcal{F}}}{\dot{\mathcal{F}}^2}. \tag{45}$$

Relating this to eq. (20) gives an expression for the braking index as a function of the semi-major axis:

$$\boxed{n_b = \frac{5}{3} - \frac{2a\ddot{a}}{\dot{a}^2}} \tag{46}$$

Since the GWs carry away energy and angular momentum from the binary and those can only come from the orbital energy and orbital angular momentum, over time the secondary will assume less energetic orbits. Looking at eq. (13) makes it clear that this means the secondary and primary are getting closer together over time. Eventually they get so close together that their event horizons merge, which means the BHs coalesce. This of course happens continuously, causing the secondary to fall into the primary following a spiral form, which is why this phenomenon is called "inspiral". An IMRI is a special case of a solar mass BH inspiraling into a intermediate mass BH, like in our case.

The mean orbital frequency $\mathcal{F}$ expresses how many cycles the secondary goes through in a given time, thus the number of cycles in a given time interval $[t_i, t_f]$ can be calculated with

$$N_{orb}(t_i, t_f) = \int_{t_i}^{t_f} \mathcal{F}(t)dt. \tag{47}$$

For the n-th harmonic and setting $t_f = t_c$ at the time of coalescence, this can be related to the number of cycles of the GW signal until the end of the signal with [32]

$$N_{GW}(t) = \int_t^{t_c} f(t)dt = nN_{orb}(t, t_c) = n\int_t^{t_c} \mathcal{F}(t)dt. \tag{48}$$

So GWs are not only a source of orbital energy loss for the binary. They also act as information carriers from whom all the relevant information needed to make statements about the nature of the inspiral and thus the DM halo can be obtained.

2.4 Dark matter and DM spikes

Now the DM can be added. DM can be modeled as particles that either do or don't interact with each other. As discussed, SIDM is needed to solve the core-cusp problem. If DM indeed self-interacts, it could behave in a similar way as baryonic matter, i.e. follow similar thermodynamic laws.

The most popular model to analyze this is the gravothermal fluid model. Here the attraction through gravity and the thermal interactions that statistically act as a repulsion effect can cancel each other with the right density and temperature. This causes the DM to exert an outward pressure on itself which dissolves the cusp and forms a core in the inner region of the DM cloud instead. A DM halo is expected for nearly every galaxy, as the structure formation of these clouds are expected to be linked with the structure formation of baryonic matter throughout the lifespan of the universe [33].

Massive objects such as BHs can accumulate more DM by capturing DM particles, causing a higher density of DM around them. The great gravitational attraction of the massive object changes the equilibrium state of the DM cloud, causing the formation of a mini-spike that can have a cuspy density distribution very locally without violating the core-cusp problem. The formation of such a spike requires a relatively slow accretion of mass of the BH as to maintain the adiabatic invariants.

The density distribution of a spherical symmetric halo around the primary as a function of the distance to it can be modeled using a simple power law $\rho \propto r^{-}\alpha$. To characterize the spike, a reference density ρ_{spike} and reference distance r_{spike} are needed, so that the density can be expressed as [34]

$$\rho_{DM}(r) = \rho_{spike} \left(\frac{r_{spike}}{r} \right)^{\alpha}. \tag{49}$$

As discussed, only the regime $r_{isco} < r < r_{inf}$ is of interest. The sphere of influence can in this case be defined as the sphere where the DM is twice the mass of the primary.

The power law dependence α on r is correlated with the initial density distribution of the DM halo before the adiabatic growth of the primary. The same power law can be applied to that initial distribution with the exponent $0 < \alpha_{ini} < 2$ for CDM. The exponent of the spike is then given by [35]

$$\alpha = \frac{9 - 2\alpha_{ini}}{4 - \alpha_{ini}} \tag{50}$$

which implies $2.25 < \alpha < 2.5$. For a uniform initial distribution where $\alpha_{ini} = 0$ this means the exponent is $\alpha = 9/4$. For a Navarro–Frenk–White (NFW) profile the initial distribution is $\alpha_{ini} = 1$, which means $\alpha = 7/3$. The NFW profile comes from N-body simulations of cold DM [36]. SIDM on the other hand leads to $\alpha = 7/4$ [37]. Other exponents are possible under different circumstances, however this work will focus on

$$\boxed{\alpha = 7/3,\ \alpha = 7/4 \text{ and } \alpha = 9/4}. \tag{51}$$

For the trajectory and energy of the orbit the simple two-body-problem needs to be expanded as now the mass of the DM has to be taken into account as well. So instead of m_1 the total mass $M(r) = m_1 + M_{DM}(r)$ needs to be used, where $M_{DM}(r)$ is the mass of the DM inside the sphere of radius r around the primary. This mass can be calculated by integrating over the DM density in the considered region

$$M_{DM}(r) = 4\pi \int_{r_{isco}}^{r} \rho_{DM}(r)\, r^2\, dr. \tag{52}$$

Evaluating this integral in the whole regime of interest gives

$$M_{DM}(r_{inf}) = 4\pi \int_{r_{isco}}^{r_{inf}} \rho_{spike} \left(\frac{r_{spike}}{r}\right)^{\alpha} r^2\, dr = 2m_1 \tag{53}$$

which gives a relation between ρ_{spike}, r_{spike}, α and m_1 [34]

$$r_{spike} = \left[\frac{(3-\alpha)0.2^{3-\alpha} m_1}{2\pi\rho_{spike}}\right]^{\frac{1}{3}}. \tag{54}$$

2.5 Dynamical friction

The secondary can now interact gravitationally with the DM particles as it moves through the spike. To understand how, we will take a closer look at open orbits, as mentioned in subsection 2.2. When considering the interaction between the secondary and individual DM particles, the secondary will assume the role of the primary object, while the DM particle becomes the secondary object. To not make the notation and jargon unnecessarily confusing, in the following the secondary will just be called BH (with mass m_{BH}) and the DM particle DMP (with mass m_{DM}).

Fig. 7 shows such a hyperbolic trajectory. In the rest frame of the BH the DMP has some initial momentum $\vec{p}_i$ while outside the BH's sphere of

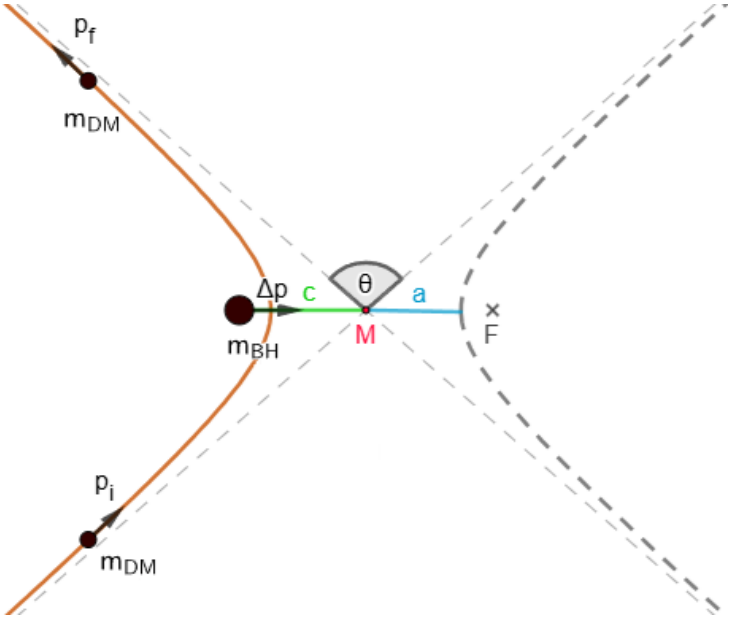

Figure 7: A hyperbolic orbit of a single DM particle around the secondary BH with midpoint M, linear eccentricity c, semi-major axis a and angle θ between the directions of the initial and final momentum $\vec{p}_i$ and $\vec{p}_f$ of the DM particle.

influence. After interacting with the BH and leaving the sphere of influence again, it has some final momentum $\vec{p}_f$. Since the conservation of momentum has to hold true, the difference in these momenta has to be transferred to the BH, so it picks up some momentum $\Delta\vec{p} = \vec{p}_i - \vec{p}_f$. Since we consider a solar mass BH as the secondary and a DMP is much lighter than a solar mass, the approximation that the center of mass is at the position of the BH and the BH is stationary throughout the encounter can once again be applied. In that approximation the absolute values of $\vec{p}_i$ and $\vec{p}_f$ are the same p_0, so the vectors are just rotated versions of each other, which leads to

$$\vec{p}_f = \begin{pmatrix} \cos(\theta) & -\sin(\theta) \\ \sin(\theta) & \cos(\theta) \end{pmatrix} \vec{p}_i \tag{55}$$

in the orbital plane. Using this, Δp can be calculated, however for later usage it's more convenient to split up $\Delta\vec{p}$ into two components, one parallel and one vertical to $\vec{p}_i$. This results in the simple expressions

$$\Delta p_\perp = p_0 |sin(\theta)| \tag{56}$$

$$\Delta p_\parallel = p_0 (1 - \cos(\theta)) \tag{57}$$

where the direction of $\Delta\vec{p}$ points towards the intersection point of the two asymptotes, which is the midpoint M.

Expanding this to a constant stream of particles along the same trajectory gives a continuous exchange of momentum i.e. a force $\vec{F}$ acting on the BH. This is a dissipative force. To calculate this force, the rate of interactions Ω needs to be known, which can be determined if the initial speed v of the DMPs and their one dimensional number density n_{1D} are known, from which the time τ between interactions can be calculated. For the parallel component of $\vec{F}$ we then have

$$\begin{aligned} F_{\parallel} &= \Omega \Delta p_{\parallel} = \frac{1}{\tau} \Delta p_{\parallel} \\ &= n_{1D}\, v\, p_0 (1 - \cos(\theta)) \\ &= n_{1D}\, m_{DM}\, v^2 (1 - \cos(\theta)), \end{aligned} \tag{58}$$

while the vertical component won't be important for further consideration. As mentioned in subsection 2.2, the shape of the orbit and by extension θ also just depend on the initial velocity and direction of motion compared to the position of the BH. To keep track of the position, the offset o can be defined as the distance between the asymptote of the incoming particle and a line parallel to that asymptote that goes through the BH. This is the closest distance the DMP would have to the BH without gravity. Through the definition of a hyperbola we can find that a and c are related to the angle ϕ between the asymptotes and the connecting line between the foci like

$$\cos(\phi) = \frac{a}{c} = \frac{1}{e}. \tag{59}$$

As $2\phi + \theta = \pi$, this relates θ to the eccentricity:

$$\begin{aligned} \frac{1}{e^2} &= \cos^2(\phi) \\ &= \frac{1}{2}(\cos(2\phi) + 1) \\ &= \frac{1}{2}(\cos(\pi - \theta) + 1) \\ &= \frac{1}{2}(1 - \cos(\theta)) \end{aligned} \tag{60}$$

which for the parallel component of the force means

$$F_{\parallel} = n_{1D}\, m_{DM}\, v^2 \frac{2}{e^2}. \tag{61}$$

Since the angular momentum L of the orbit is directly correlated with o, m_{DM} and v, it can be used to find the correlation between e, o and v. The eccentricity as function of the angular momentum and energy of the system is given by [38]

$$e = \sqrt{1 + \frac{2E_{orb}L_{orb}^2(m_{BH} + m_{DM})}{(m_{BH}\, m_{DM})^3}}. \tag{62}$$

And since the BH is initially static, both the orbital energy and the angular momentum are solely determined my the DMP. As v is the velocity of the DMP outside the sphere of influence where $E_{pot} \ll E_{kin}$, the orbital energy can be approximated as the initial kinetic energy of the DMP, while the angular momentum is given classically by $\vec{r} \times \vec{p}_{DM}$ where $\vec{r}$ is the vector pointing from the BH to the DMP. We then have

$$\begin{aligned} E_{orb} &= \frac{1}{2} m_{DM} v^2 \\ L_{orb} &= m_{DM} v\, o. \end{aligned} \tag{63}$$

Also $m_{DM} \ll m_{BH}$, so $m_{DM} + m_{BH} \approx m_{BH}$, which simplifies eq. (62) to

$$\begin{aligned} e &= \sqrt{1 + \frac{m_{DM} v^2 (m_{DM} v\, o)^2 m_{BH}}{(m_{BH}\, m_{DM})^3}} \\ &= \sqrt{1 + \frac{o^2 v^4}{m_{BH}^2}}. \end{aligned} \tag{64}$$

Plugging this into eq. (61) results in an expression for the parallel component of the force that only involves the initial parameters of the DMP:

$$F_{\parallel} = n_{1D}\, m_{DM}\, v^2 \frac{2m_{BH}^2}{m_{BH}^2 + o^2 v^4}. \tag{65}$$

Now we can expand this further by considering all possible constant streams of DMPs that have the same offset o. How close together these streams are can be expressed by a second one-dimensional number density n_{st} which, together with the number density n_{1D} of the DMPs in each steam, defines the two-dimensional number density $n_{2D} = n_{1D} \cdot n_{st}$ of the DM. To get the total interactions per second all the streams have to be added up, or in the continuous case integrated over all possible directions. The rate of interactions is then

$$\Omega = \int_0^{2\pi} n_{2D} v\, o\, d\varphi = 2\pi n_{2D} v\, o \tag{66}$$

which for the force means

$$F_{\parallel} = 4\pi n_{2D}\, m_{DM}\, v^2\, \frac{o\, m_{BH}^2}{m_{BH}^2 + o^2 v^4}. \tag{67}$$

Since the configuration is now rotationally symmetric, all the orthogonal components of the force cancel each other, which makes clear why they don't need to be taken into account.

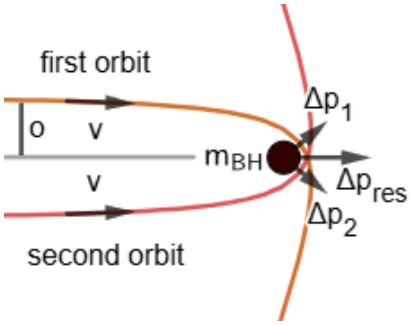

Figure 8: A visualization of the orthogonal components of the DF force canceling for a uniform density distribution, created with GeoGebra.

Fig. 8 shows how for every DMP with offset o and velocity v in one direction there exists another DMP with the same velocity and offset in the opposite direction. The first orbit results in a change of Δp_1, the second results in Δp_2. Assuming the same initial velocity v for both DMPs, both the parallel and orthogonal components are the same, with the orthogonal components pointing in opposite directions. This results in the total change of momentum $\Delta p_{res} = \Delta p_1 + \Delta p_2$ where the orthogonal components cancel and the parallel components add up. Expanding this to DMP streams and assuming the same number density for both streams, the same is true for the force acting on the BH, so the DF force is parallel to $\vec{v}$.

Eq. (67) can be expanded further to a case of a uniform three-dimensional DM cloud by integrating the force over all the relevant offsets o. To do that, the third and last number density n_o of the DMPs along the direction of increasing o is needed. Together with n_{2D} this gives the overall three-dimensional DMP number density $n_{3D} = n_{2D} \cdot n_o$, and the force is then given by

$$
\begin{aligned}
F_{\parallel} &= 4\pi n_{3D}\, m_{DM}\, v^2 \int_0^{o_{max}} \frac{o\, m_{BH}^2}{m_{BH}^2 + o^2 v^4} do. \\
&= 4\pi\rho\, v^2 \frac{m_{BH}^2}{2v^4} \ln\left(\frac{o_{max}^2 v^4}{m_{BH}^2} + 1\right) \\
&= \frac{4\pi\rho\, m_{BH}^2}{v^2} \ln(\Lambda)
\end{aligned}
\tag{68}
$$

where the uniform DM density $\rho = n_{3D} m_{DM}$ was introduced and the Coulomb logarithm $log(\Lambda)$ was defined as

$$
\Lambda = \sqrt{\frac{o_{max}^2 v^4}{m_{BH}^2} + 1}. \tag{69}
$$

Since the integral in eq. (68) diverges for $o_{max} \to \infty$, some other value needs to be chosen depending on the considered case. For IMRIs, some values in the literature for $\ln(\Lambda)$ are 3, 10 and $\ln(m_1/m_2)$ [32, 39, 40]. Here the latter definition $\Lambda = m_1/m_2$ is used.

As clearly can be seen in eq. (68), unlike a typical friction force the DF does not increase, but instead decreases with higher relative velocities v. This also becomes clear when considering another viewpoint on DF: If a massive object moves through a field of stars or in this case DMPs, it will attract them, which causes them to bunch together behind the massive object. This results in a higher gravitational force antiparallel to the direction of motion than parallel to it. The faster the object moves, the less time it has to accumulate stars or DMPs behind it, and at the same time it moves further away quicker from the bunched together wake, resulting in less gravitational attraction. Both these effects cause the antiparallel force to be weaker the faster the object is moving relative to the field.

2.5.1 DF in the BH binary

As the secondary moves through the DM spike of the primary, it experiences DF. Until now only DMPs that share the same velocity were considered, which is not the case for the spike. When considering a cloud of DMPs with different velocities it's not enough to just calculate the mean velocity and use that as v in eq. (68). Instead the velocity distribution needs to be taken into account completely, which can be done by expanding the DM density [32]:

$$
F_{\parallel} = \frac{4\pi\rho\, \xi(v)\, m_{BH}^2}{v^2} \ln(\Lambda)\,. \tag{70}
$$

For IMRIs, ρ is just the DM density $\rho_{DM}(r)$ dependent on the distance between secondary and primary, and v the velocity of the secondary through the DM spike. $\xi(v)$ can be estimated like in [41] and [31] with

$$\rho_{DM}(r)\xi(v) = 4\pi \int_0^v v'^2 f\left(\Psi(r) - \frac{1}{2}v'^2\right) dv' \tag{71}$$

with the relative potential $\Psi(r)$. This accounts for the DM moving slower than the secondary, which in some circumstances can be a good enough approximation. To also include higher velocities of DMPs, the following equation needs to be used [42]:

$$F_{\parallel} = \frac{4\pi\rho(r)\, m_{BH}^2}{v^2} \left[\alpha(v) \ln(\Lambda) + \beta(v) + \delta(v)\right] \tag{72}$$

with

$$\begin{aligned} \alpha(v) &= 4\pi \int_0^v f(v')v'^2 dv' \\ \beta(v) &= 4\pi \int_v^{v_{esc}} f(v')v'^2 \left[\ln\left(\frac{v'+v}{v'-v}\right)\right] dv' \\ \delta(v) &= 4\pi v \int_v^{v_{esc}} f(v')(-2v')dv'. \end{aligned} \tag{73}$$

Again, α just accounts for the slower moving DM, while including higher velocities requires $\beta(v)$ and $\delta(v)$. Assuming $\alpha(v) = m_{BH}\xi(v)$ and $\beta(v) = \delta(v) = 0$ leads to eq. (70) again. Since $\vec{v}$ now describes the motion of the BH instead of that of the DMPs, the direction of the force is now antiparallel to $\vec{v}$. Putting all this together gives three approximations for the DF force:

$$\boxed{\vec{F}_{DF} = -\frac{4\pi\rho\,\xi(v)\, m_{BH}^2}{v^2} \ln(\Lambda)\, \frac{\vec{v}}{v}} \tag{I}$$

$$\boxed{\vec{F}_{DF} = -\frac{4\pi\rho(r)\, m_{BH}^2}{v^2}\, \alpha(v) \ln(\Lambda)\, \frac{\vec{v}}{v}} \tag{II}$$

$$\boxed{\vec{F}_{DF} = -\frac{4\pi\rho(r)\, m_{BH}^2}{v^2} \left[\alpha(v) \ln(\Lambda) + \beta(v) + \delta(v)\right] \frac{\vec{v}}{v}} \tag{III}$$

Since the DF force is antiparallel to the secondary's velocity, some of the secondary's kinetic energy is transferred to the DM spike which can be seen as an overall loss of orbital energy for the BH binary. The power can be

calculated with the simple relation of energy being a force over a distance $E = F \cdot s$, hence

$$\dot{E}_{DF} = \dot{F}_{DF} \cdot s + F_{DF} \cdot \dot{s} \approx F_{DF}\, v \tag{74}$$

assuming the change of force is small compared to the velocity. This adds up with the energy loss due to the GW emission itself:

$$\frac{dE}{dt} = \dot{E}_{tot} = \dot{E}_{GW} + \dot{E}_{DF}. \tag{75}$$

This higher energy loss causes a faster inspiral, which means the DM has an impact on the frequency evolution of the BH and thus also of the GW signal. The DF interaction with the DM causes a change ΔN in the number of cycles in eq. (48) compared to a case without DM [31]:

$$\boxed{\Delta N(t) = N_{vacuum}(t) - N_{tot}(t)} \tag{76}$$

This phenomenon is called dephasing. From that the dephasing index can be defined as [31]

$$\boxed{n_d = \frac{d\,\ln(\Delta N)}{d\,\ln(\mathcal{F}_{tot})}} \tag{77}$$

Additionally, both GWs and DF can change the shape of an orbit. With DF involved this tends to make the orbit more circular, decreasing the eccentricity [41].

The comparison of the relative differences between eqs. (I) and (II) as well as between eqs. (II) and (III) and their impact on h_c, ΔN, n_d and n_b under different conditions is the goal of this thesis.

3 Implementation

To compare the differences, the IMRIpy[6] simulation by Niklas Becker was used to model an IMRI under different conditions and numerically produce some observables. The exponent α, the spike density ρ_{spike}, primary mass m_1, secondary mass m_2, initial radius R_0, eccentricity e and the distance D to the system have to be defined. From α, m_1 and ρ_{spike}, r_{spike} can be calculated using eq. (**??**) [34]. Using all these values the host system with DM spike and the initial KO can be defined. From there, the system can be evolved with

[6] `https://github.com/DMGW-Goethe/imripy`

```
imripy.inspiral.Classic.Evolve(hs, ko_initial, opt=options);
```

Here, options is an object specifying the functionality of different functions and classes in the code. With is, the

```
imripy.inspiral.forces.DynamicalFriction()
```

class can be specified to use or not use the phase space description, as well as ignoring or not ignoring higher velocities. This can be used to specify which of the eqs. (I)-(III) ought to be used my the code.

After setting up the system, the n-th harmonic GW signal can be simulated with

```
imripy.waveform.h_n(n, hs, ev);
```

This work will be restricted to $n = 2$. This function returns three arrays, one containing the frequencies, tho other two containing $\tilde{h}_+(f)$ and $\tilde{h}_\times(f)$ respectively. From these arrays, the characteristic strain can be calculated with eq.(??).

To calculate ΔN, the time evolution is simulated with and without the DM spike. The numbers of cycles until the coalescence can be obtained with

```
imripy.waveform.N_cycles_n(n, hs, ev);
```

from which ΔN can be calculated with eq. (??). To calculate from that the dephasing index with eq. (??), the

```
np.gradient()
```

function can be used. The braking index can be obtained with

```
imripy.waveform.BrakingIndex(hs, ev);
```

Most plots look very similar for the different equations (I)-(III). For that reason, I decided against showing curves for different equations in the same plots, as they would just mostly overlap. To get a feeling for the differences of these observables when using the different equations, they were instead simply subtracted and plotted. The absolute values of the observables and their differences are plotted, so that logarithmic axes can be used. To compare the equations, hs and ev as well as all other relevant objects were turned into arrays with the index indicating a corresponding equation.

To analyze what values influence this difference the most, all the previously

defined starting values were varied. For the base configuration similar values to [39] were taken with $\rho_{spike} = 226 M_\odot/pc^3$, $m_1 = 10^3 M_\odot$, $m_2 = 1 M_\odot$, $R_0 = 100 r_{isco}$ and $e = 0$. The distance D from the observer to the binary was set to $500 Mpc$ and not varied. Deviating from these base values, two additional values for each of the parameters were defined. Tab. 1 lists all the defined values.

ρ_{spike}	m_1	m_2	R_0	e
$0.027 M_\odot/pc^3$	$1 \cdot 10^3 M_\odot$	$1 M_\odot$	$1000 r_{isco}$	0
$226 M_\odot/pc^3$	$1 \cdot 10^4 M_\odot$	$20 M_\odot$	$100 r_{isco}$	0.4
$2 \cdot 10^6 M_\odot/pc^3$	$5 \cdot 10^4 M_\odot$	$100 M_\odot$	$30 r_{isco}$	0.8

Table 1: All the used values to analyze their effect on the differences eqs. (I)-(III) make for the simulated observables.

The values cannot be subtracted by simply subtracting the arrays, as in general the corresponding frequency values are different. Thus, the interval where both frequency arrays overlap was determined, and the value functions interpolated over that interval. The difference of the frequency arrays also means that a standard interpolation causes the distance of the two functions for different frequency values to vary. This is shown in fig. 9.

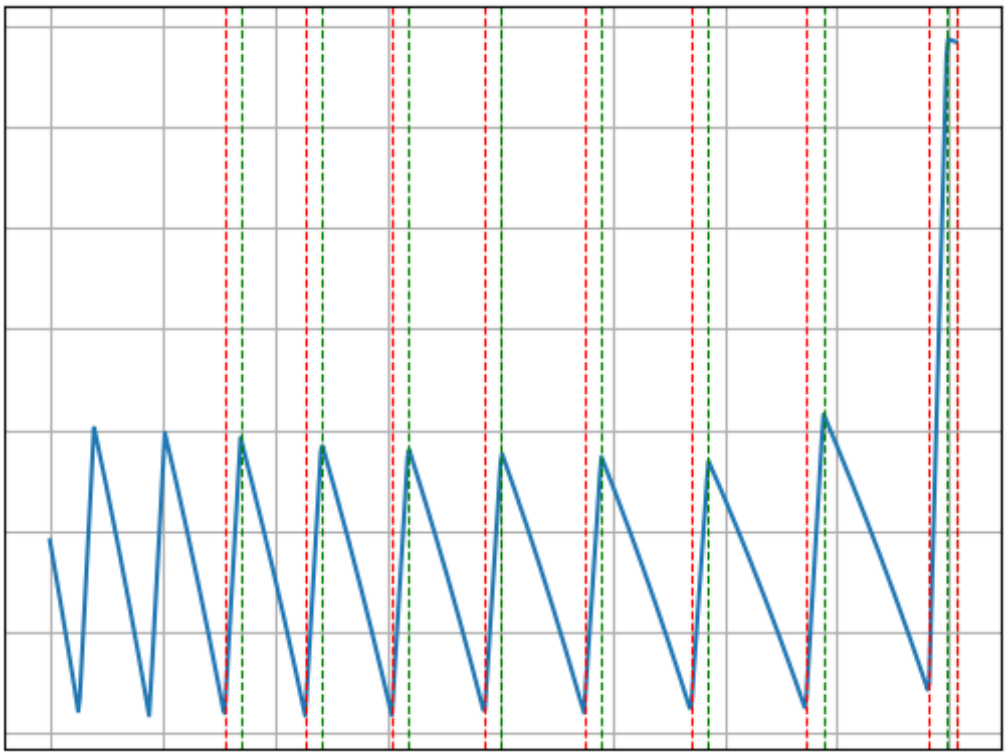

Figure 9: Here the effect of linear interpolation on the difference of two numerical functions is seen. The green vertical lines show the x-values of one of the functions, the red ones the x-values of the other one. It can be seen that the spikes are exactly at the position of these x-values, showing that this behavior is due to the x-value arrays not being continuous.

To mitigate this effect as much as possible, the

`scipy.interpolate.interp1d()`

function was used with the *kind="cubic"* option. This also acts as a kind of fitting, predicting the behavior of the values in-between the values of the frequency arrays. Note that this does not entirely get rid of all the numerical errors, as seen in the results.

4 Results

The code can plot a lot of different quantities relevant for the system. To prevent excessive length of this work, some plots will only be shown for varying ρ_{spike}, and will be left out later except if something interesting can be seen. Additionally, the base eccentricity of 0 means that there is no difference between +- and ×-polarization and thus only the characteristic strain of the +-polarization is shown.

4.1 Varying ρ_{spike}

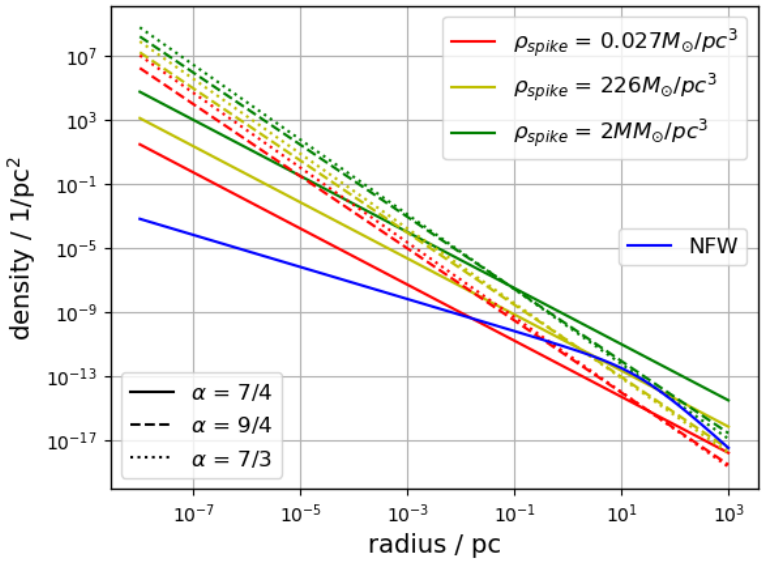

Figure 10: The density profile for the different values for ρ_{spike}. This plot is rather trivial, as a higher ρ_{spike} means a higher density at every point in the spike, thus an increase in ρ_{spike} corresponds to a upward shift in the plot. The slope of the curve is simply given by α. A NFW profile is included for comparison.

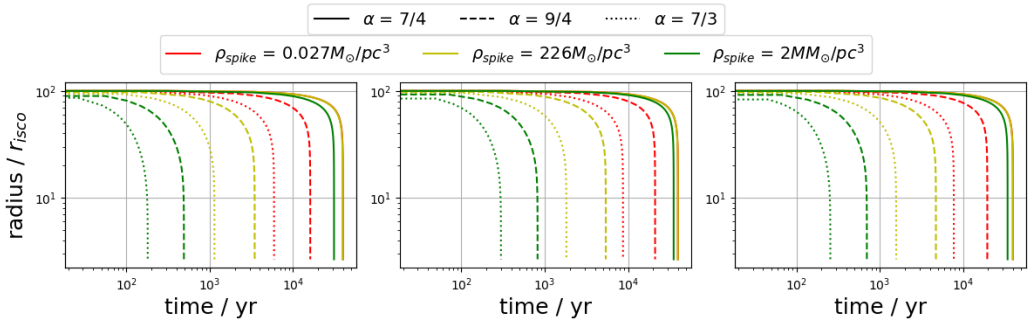

Figure 11: Here the temporal evolution of the radius is shown for eq. (I) on the left, (eq. II) in the middle and eq. (III) on the right. It can be seen that, not surprisingly, higher DM densities result in a faster inspiral. At the same time, higher values of α seem to favor faster inspirals as well.

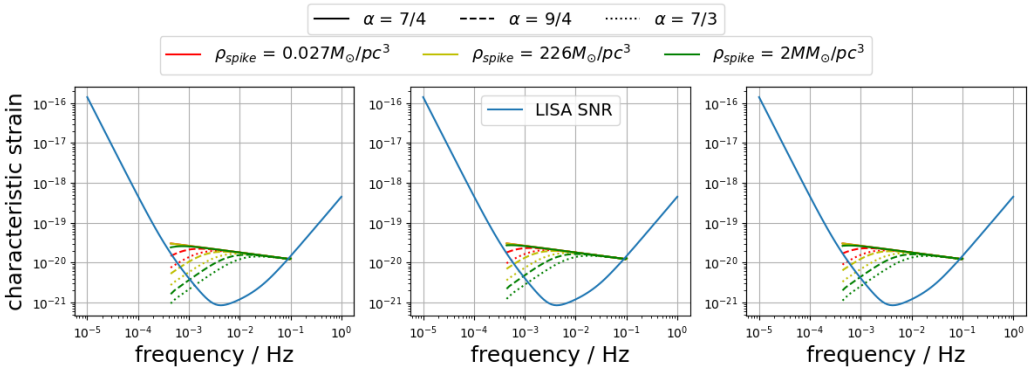

Figure 12: The characteristic strain for eq. (I) on the left, eq. (II) in the middle and eq. (III) on the right. Since the eccentricity is 0, the wave is polarized circularly, thus both polarizations have the same characteristic strain. The shape of the curves is relatively the same, but shifted towards lower frequencies for lower densities. As can be seen in the following, the same is true for most of the other plots as well. The LISA SNR curve is included as well, and it can be seen that GWs from the modeled system could indeed be detected.

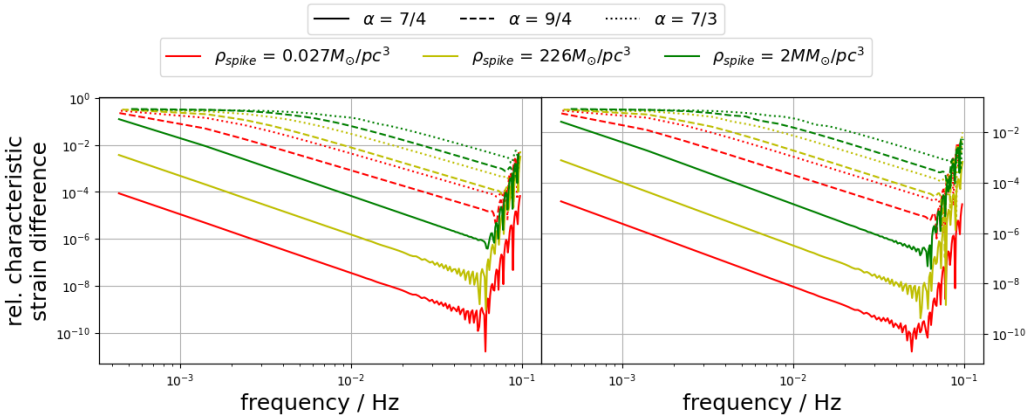

Figure 13: The relative differences in the characteristic strain caused by using the different equations (on the left the comparison between eqs. (I) and (II), on the right between eqs. (II) and (III)). As to be expected, a lower density results in less difference, as in this case DF is in general less significant for the signal compared e.g. the orbital energy loss caused by the GWs themselves. Interestingly, the differences appear to be capped at around 12% for eqs. (I) and (II) and 10% for eqs. (II) and (III). A downward trend for higher frequencies is apparent. At around $7 \cdot 10^{-2}$ this trend seems to reverse. However, the very strong numerical errors starting at around the same frequency have to be noted, making the meaningfulness of this reversal questionable.

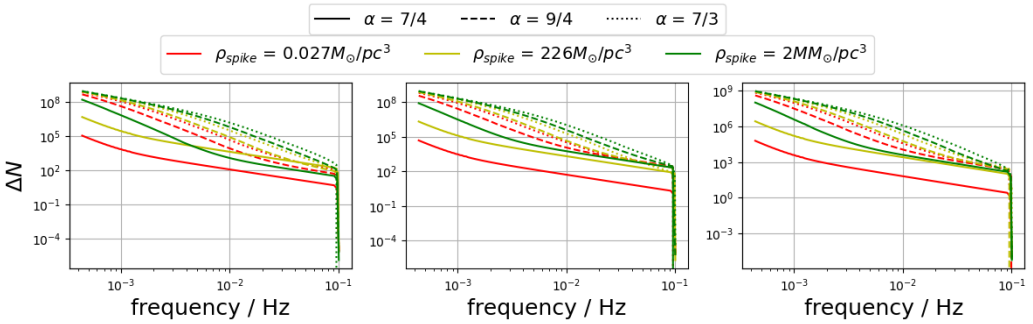

Figure 14: The dephasing for eq. (I) on the left, eq. (II) in the middle and eq. (III) on the right. Again, it is no surprise that higher densities result in stronger dephasing.

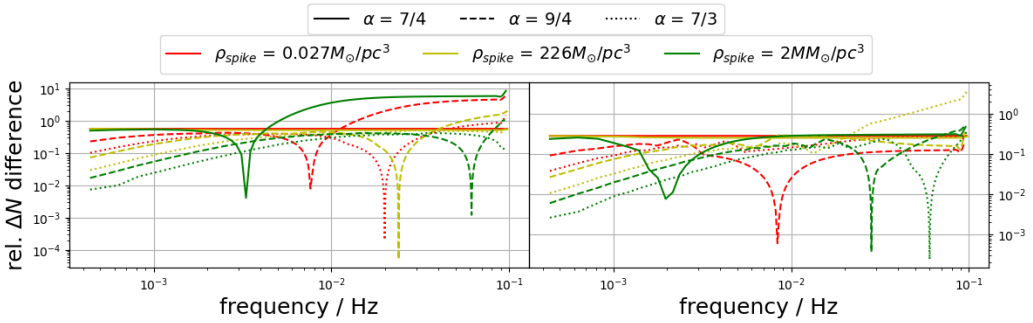

Figure 15: The relative difference of the dephasing when comparing eq. (I) with (II) on the left, and eq. (II) with (III) on the right. As the absolute value is plotted, the spike-like valleys correspond to sign changes, thus marking the frequencies where the dephasing is the same for both equations. Also, the vast magnitude of the difference has to be noted, with some curves reaching up to 1000% difference. Especially the differences between eqs. (I) and (II) seems to tend to very high values at higher frequencies.

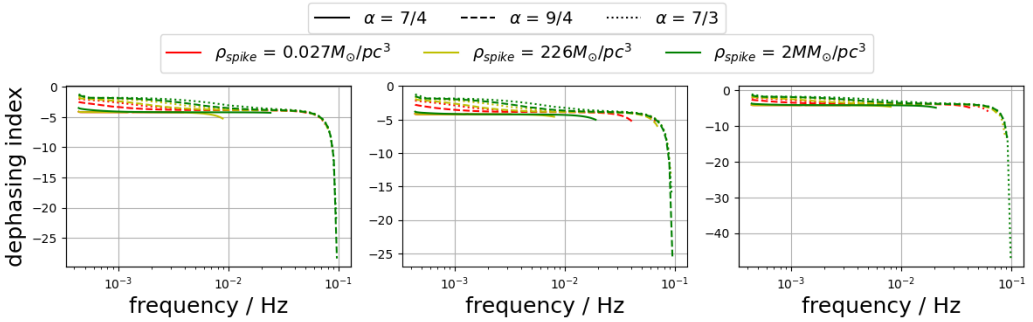

Figure 16: The dephasing indes for eq. (I) on the left, eq. (II) in the middle and eq. (III) on the right. As with the dephasing itself, lower densities lead to smaller dephasing indices.

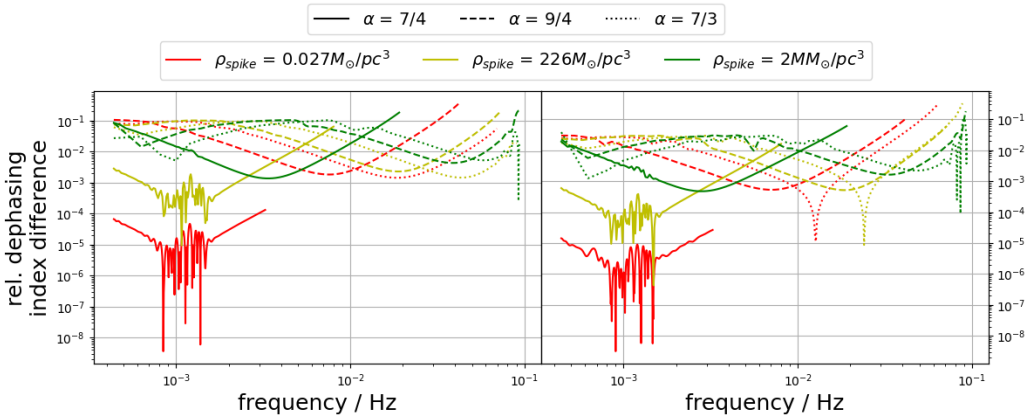

Figure 17: The relative difference of the dephasing index when comparing eq. (I) with (II) on the left, and eq. (II) with (III) on the right. Ignoring the errors around $f = 10^{-3}Hz$, the curves again seem very similar, but shifted towards lower frequencies for smaller α and ρ_{spike}.

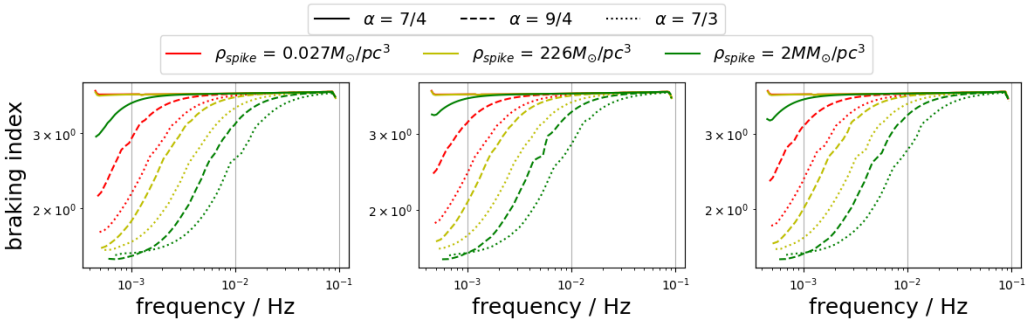

Figure 18: The braking index for eq. (I) on the left, eq. (II) in the middle and eq. (III) on the right.

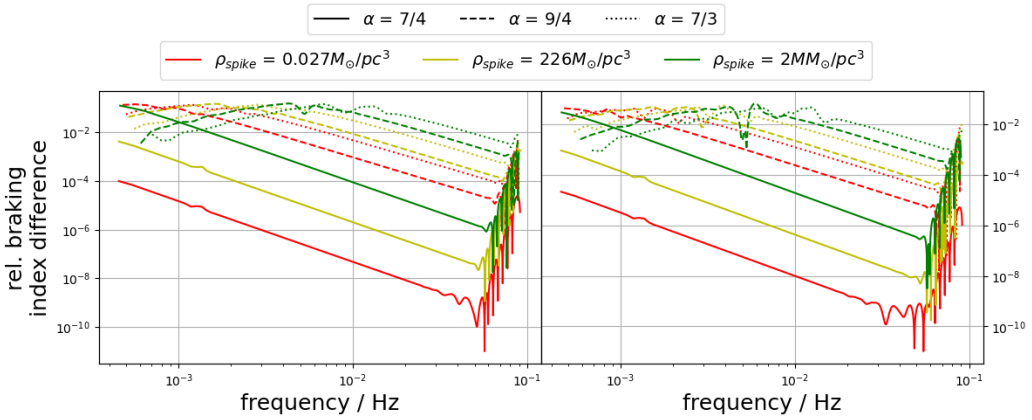

Figure 19: The relative difference of the braking index when comparing eq. (I) with (II) on the left, and eq. (II) with (III) on the right. One again, the similarities of the curves can be seen, and curves with lower α or ρ_{spike} seem to be shifted towards lower frequencies. The curves where the maximum can be seen have that maximum at around 10% difference.

4.2 Varying m_1

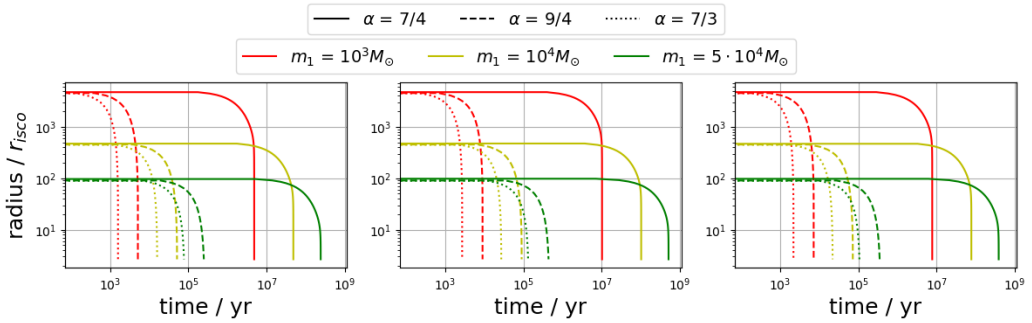

Figure 20: The evolution of the radius for eq. (I) on the left, eq. (II) in the middle and eq. (III) on the right. Varying m_1 also varies r_{isco}. R_0 had to be modified as well to make the simulation work, and is 100 times r_{isco} for $m_1 = 5 \cdot 10^4 M_\odot$.

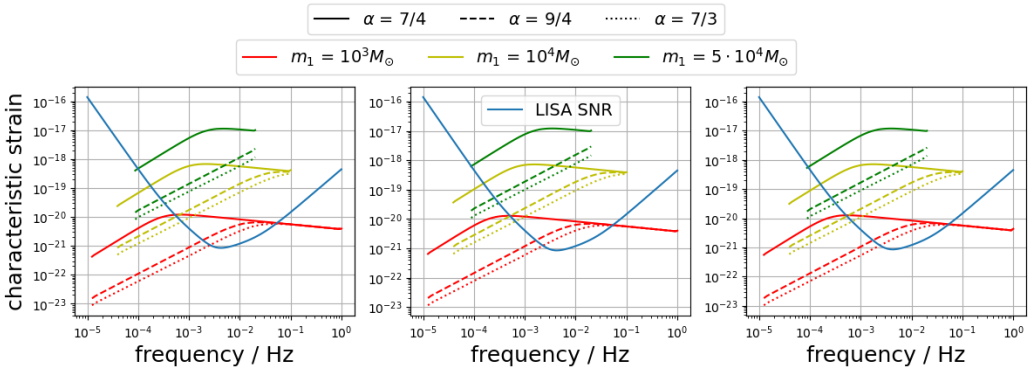

Figure 21: The characteristic strain for eq. (I) on the left, eq. (II) in the middle and eq. (III) on the right. It can be seen that the GW signal is more pronounced for higher primary masses. All signals are still detectable.

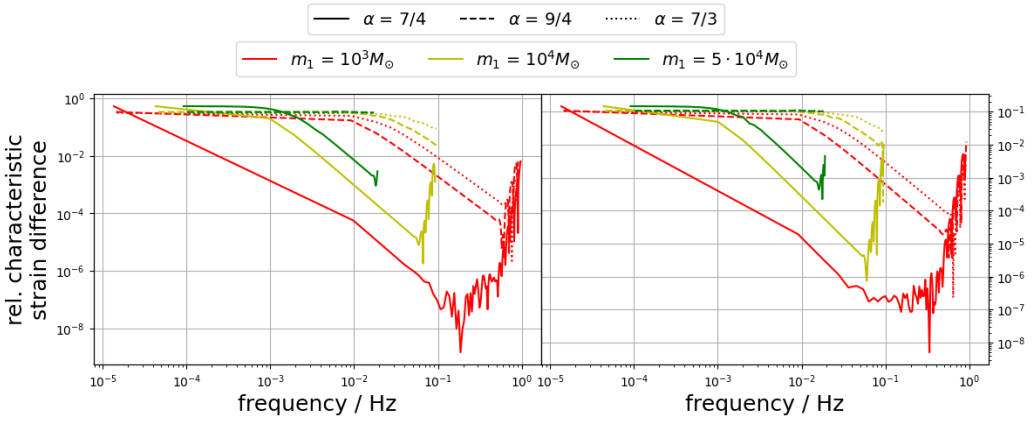

Figure 22: The differences in the characteristic strain when comparing eq. (I) with (II) on the left, and eq. (II) with (III) on the right. Again, the curves seem to tend towards a maximum for lower frequencies, this time it's about 70% for eqs. (I) and (II), and 10% for eqs. (II) and (III). Higher masses result in higher differences, and at the same time the the shift towards lower frequencies for lower α and m_1 can be seen.

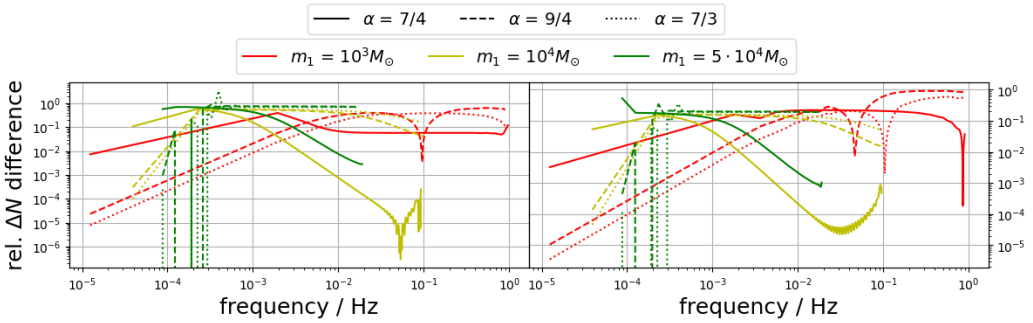

Figure 23: The differences in the dephasing when comparing eq. (I) with (II) on the left, and eq. (II) with (III) on the right. Differences of up to 100% are reached. Some weird behavior can be seen at around $f = 1.5 \cdot 10^4 Hz$, which is probably caused by numerical issues, as $m_1 = 5 \cdot 10^4 M_\odot$ caused some issues in general. Aside from that, higher masses for the most part resulted in higher differences.

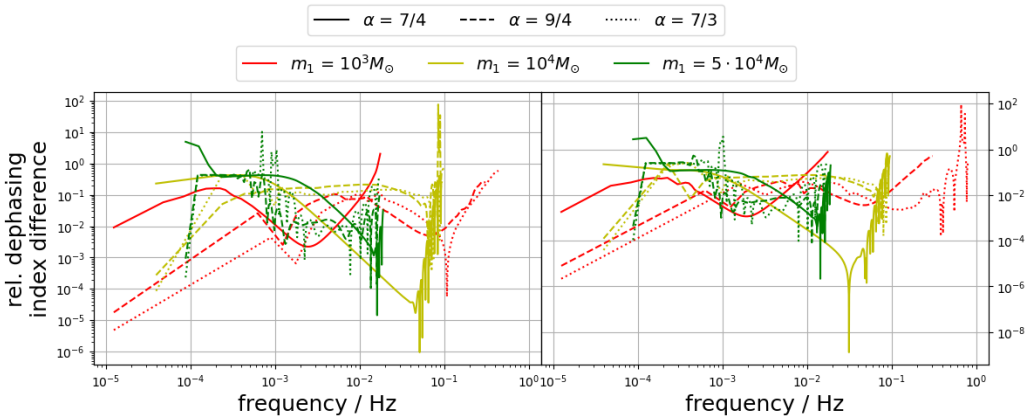

Figure 24: The differences in the dephasing index when comparing eq. (I) with (II) on the left, and eq. (II) with (III) on the right. The differences seem to be capped at around 75%, with the spikes of up to 10000% most likely stemming from numerical errors. It's difficult to be sure, but higher masses seem to result in higher differences. Once again, the shapes of the curves are similar but shifted towards lower frequency for lower masses.

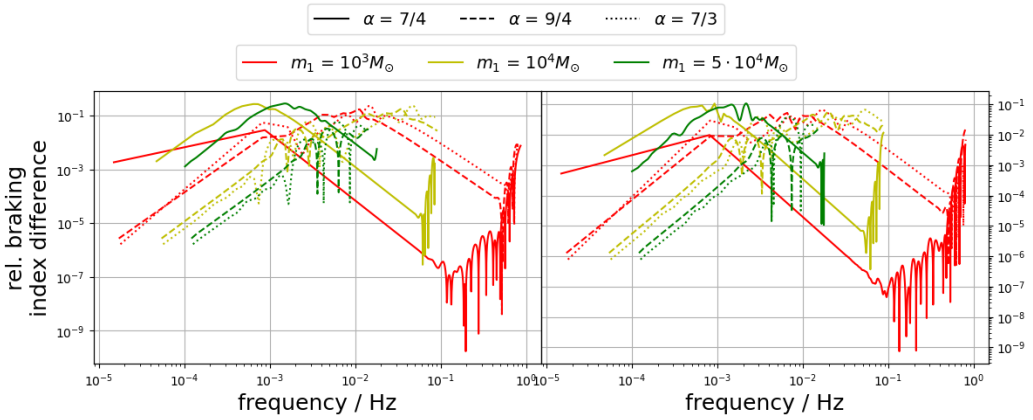

Figure 25: The differences in the braking index when comparing eq. (I) with (II) on the left, and eq. (II) with (III) on the right. The cueves have a maximum at around 10%, and a shift towards lower frequencies for smaller masses can be seen.

4.3 Varying m_2

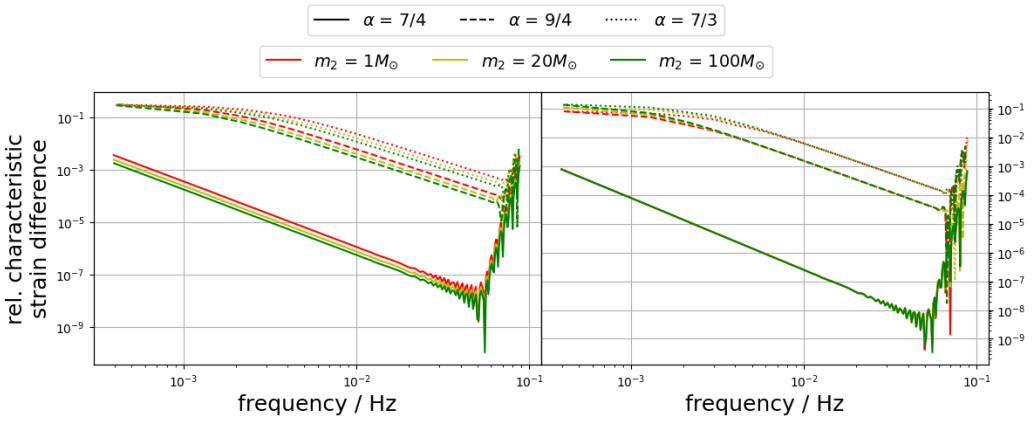

Figure 26: The differences in the characteristic strain when comparing eq. (I) with (II) on the left, and eq. (II) with (III) on the right. Again, there seems to be a cap at around 12% on the left, and 10% on the right side. Higher masses result in lower differences. This could mean that m_2 is more relevant for DF than it is for the GW energy flux.

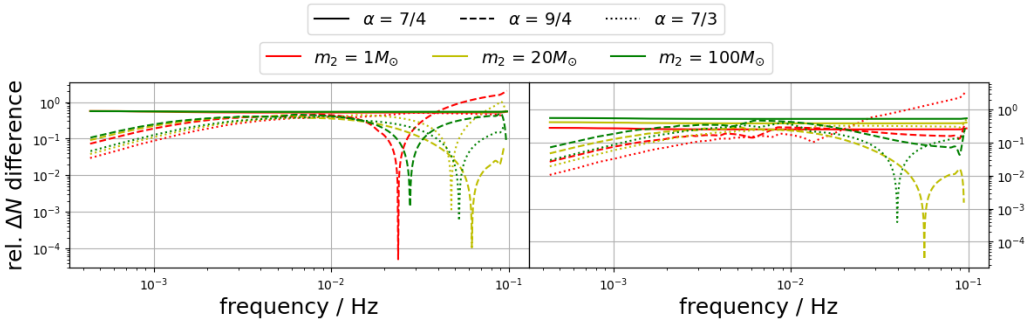

Figure 27: The differences in the dephasing when comparing eq. (I) with (II) on the left, and eq. (II) with (III) on the right. Most of the differences reach up to about 70%, with only two curves surpassing this value to up to 120%. Here, higher masses mostly result in higher differences.

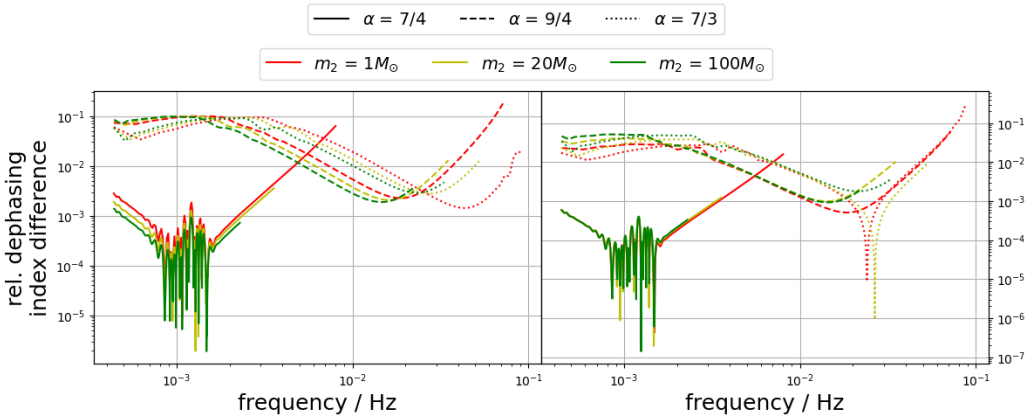

Figure 28: The differences in the dephasing index when comparing eq. (I) with (II) on the left, and eq. (II) with (III) on the right. The left side reaches up to about 10%, the right side roughly 7%. Here, the frequency shift for $\alpha = 9/4$ and $\alpha = 7/3$ can be seen pretty nicely. At the same time there is not frequency shift for $\alpha = 7/4$ here. On the left side, higher masses result in curves shifted towards lower frequencies while simultaneously causing lower differences. On the right side, all masses result in roughly the same differences, but at slightly different frequencies.

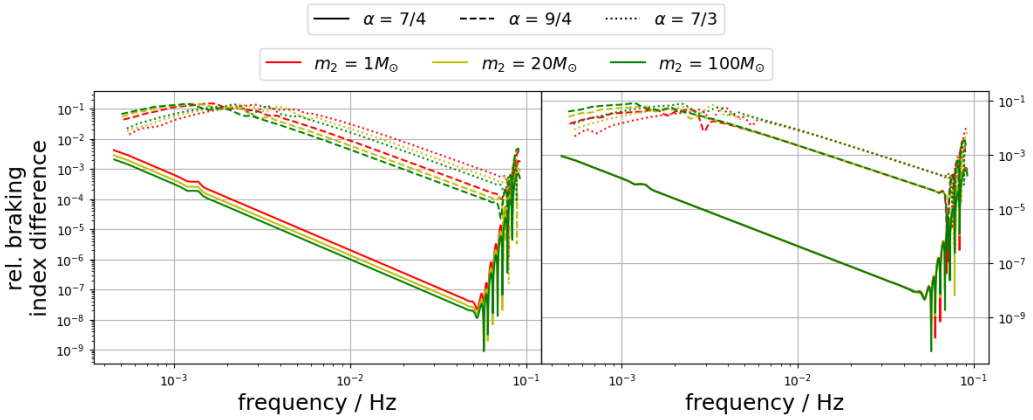

Figure 29: The differences in the braking index when comparing eq. (I) with (II) on the left, and eq. (II) with (III) on the right. Higher masses result in lower differences. Here, the curves behave in exactly the same manner as for the dephasing index.The cap is at just over 10% for the left, and around 8-9% on the right side.

4.4 varying R_0

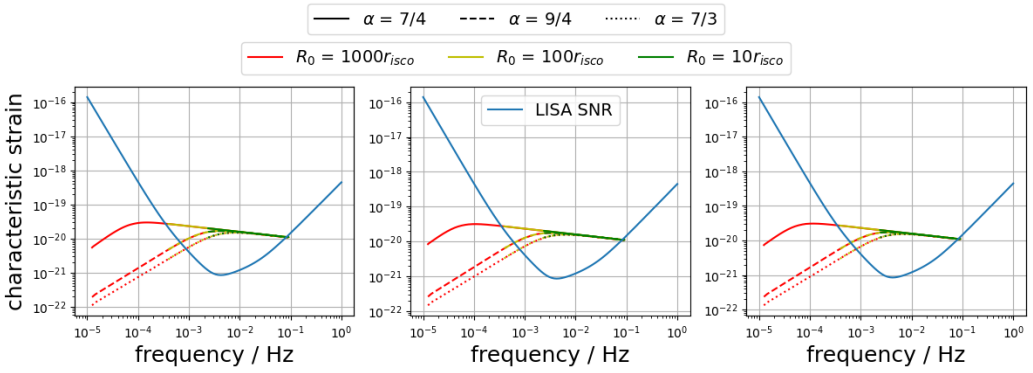

Figure 30: The characteristic strain for eq. (I) on the left, eq. (II) in the middle and eq. (III) on the right. It can be seen, that the evolution for different R_0 is the same, just with different starting points, as is expected.

As only the dephasing is influenced by different initial radii, it will be the only observable shown here. For the characteristic strain and braking index the curves are equivalent to the curves of the base configuration in all the other plots shown.

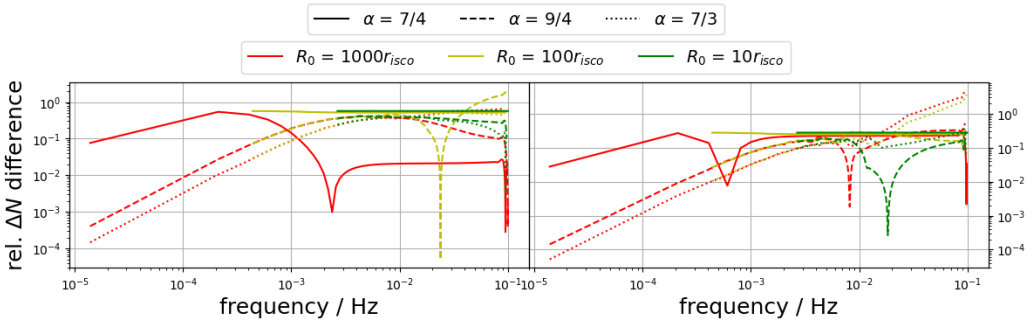

Figure 31: The differences in the dephasing when comparing eq. (I) with (II) on the left, and eq. (II) with (III) on the right. The differences stay just below 80% on the left and 20% on the right side. For $\alpha = 7/4$ and $\alpha = 9/4$, higher radii result in slightly smaller differences, while for $\alpha = 7/3$ the opposite seems to be the case.

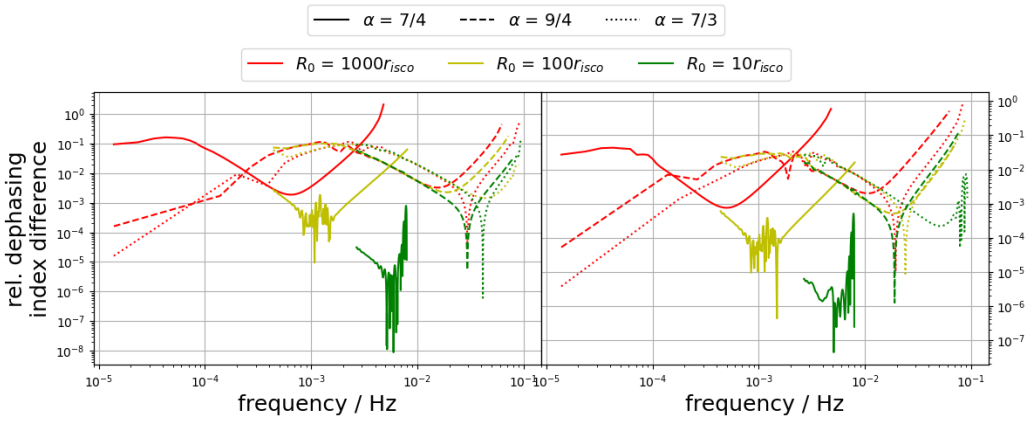

Figure 32: The differences in the dephasing index when comparing eq. (I) with (II) on the left, and eq. (II) with (III) on the right. The differences are bigger for higher values of R_0, and at the same time a shift towards lower frequencies can be seen for higher radii as well as for lower values of α.

4.5 Varying e

For the eccentricity I ran into some issues that I sadly wasn't able to fully resolve, partly due to the very long simulation times for non-zero eccentricities. Thus still only the plus-polarization will be shown here, even though

for an eccentric orbit the different polarizations could become relevant.

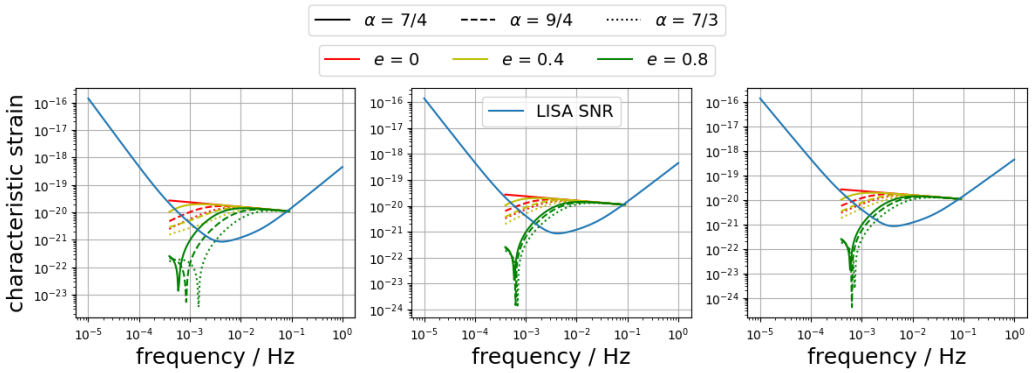

Figure 33: The characteristic strain for eq. (I) on the left, eq. (II) in the middle and eq. (III) on the right. Here, a change in sign can be seen. It is interesting to see that more accurate equations seem to focus the point of that change for different α.

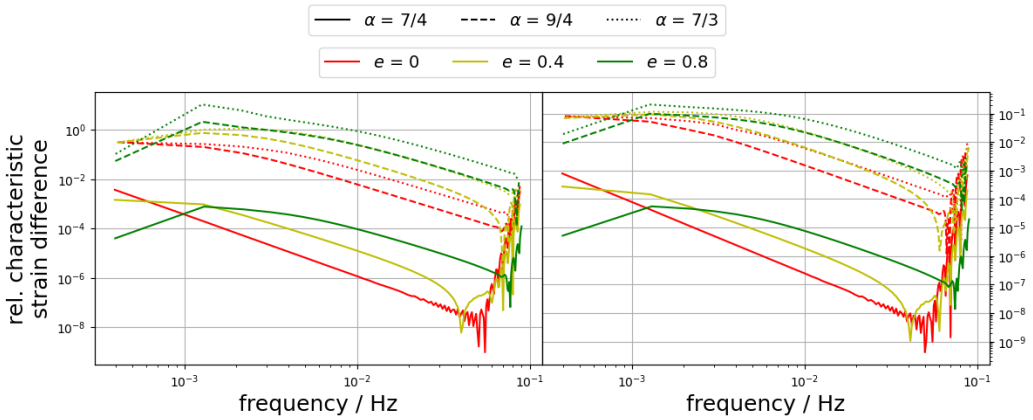

Figure 34: The differences in the characteristic strain when comparing eq. (I) with (II) on the left, and eq. (II) with (III) on the right. For lower frequencies, smaller e correlate to smaller differences, however for higher frequencies that relation reverses. With non-zero eccentricity, the caps of 12 and 10% are finally exceeded.

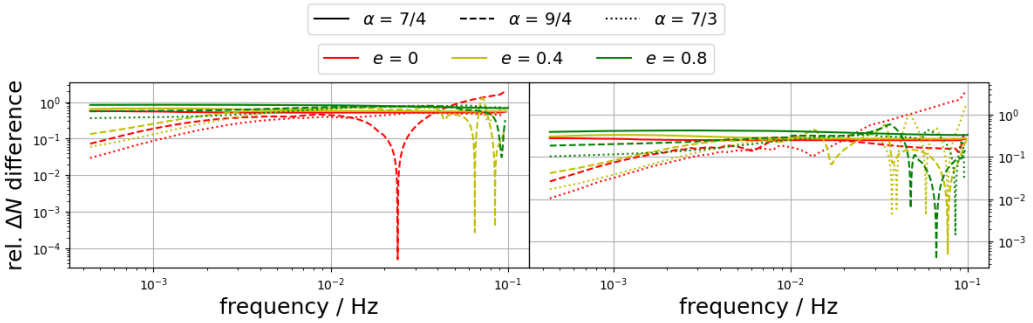

Figure 35: The differences in the dephasing when comparing eq. (I) with (II) on the left, and eq. (II) with (III) on the right. Here as well the eccentricities increase the differences, reaching up to 100% difference on the left, and around 30% on the right side.

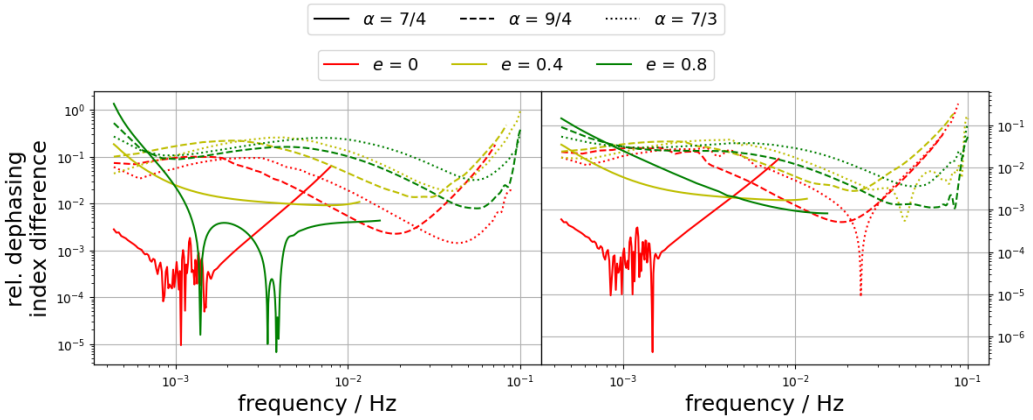

Figure 36: The differences in the dephasing index when comparing eq. (I) with (II) on the left, and eq. (II) with (III) on the right. The difference is greater for higher eccentricities.

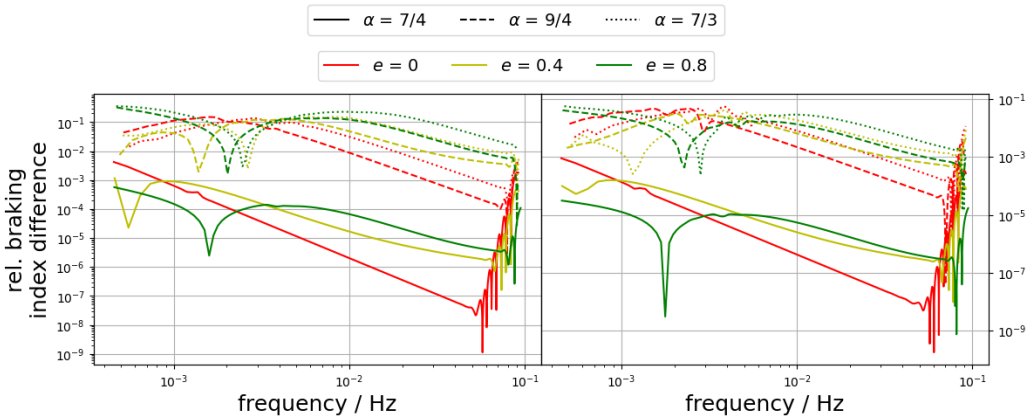

Figure 37: The differences in the braking index when comparing eq. (I) with (II) on the left, and eq. (II) with (III) on the right. For low frequencies, lower eccentricities seem to cause higher differences, but once again this relation reverses for higher frequencies.

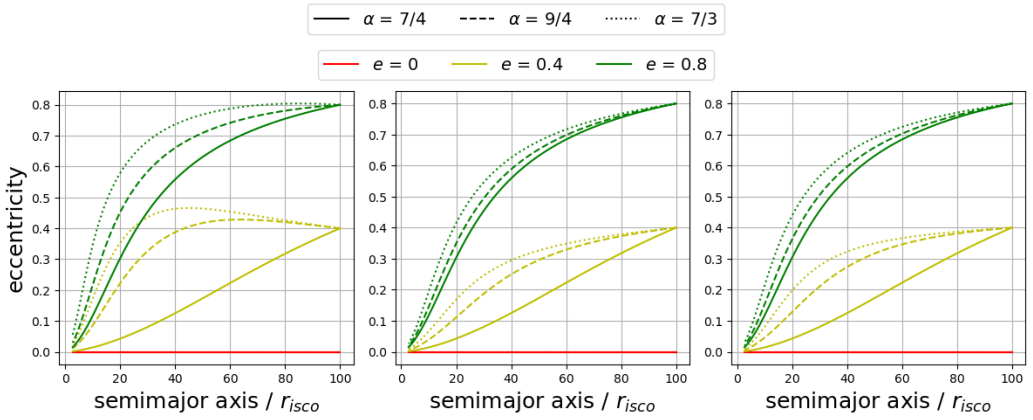

Figure 38: The eccentricity evolution for eq. (I) on the left, eq. (II) in the middle and eq. (III) on the right. With eq. (I), an eccentrification is expected for the outer regions, while the newer equations predict a circularization of the orbit.

5 Conclusion

The goal of this thesis was to quantize the effects that different DF modulations have on some observable quantities of GWs generated by IMRIs with DM spikes. These observables are a good (or perhaps the only) way to probe DM and its properties, including the question weather DM is self-interacting. Extracting information about the DM from GWs is a delicate endeavor, raising the importance of very precise models. In this work it was shown that the differences between eqs. (I), (II) and (III) are indeed substantial for the considered system.

In summary, the differences for the characteristic strain are noticeably bigger for high values of ρ_{spike}, m_1 and e and low values of m_2.

For ΔN, the differences are big for high values of m_1, m_2 and e and low values of ρ_{spike}.

The differences of the dephasing idex are big for high values of ρ_{spike}, m_2 and e and low values of R_0.

Lastly, the braking index difference is big for high values of ρ_{spike} and e and low values of m_2.

The difference between the observables for eq.(I) and eq.(II) are in general larger than the ones for eq.(II) and eq.(III). However, the latter are still relatively significant. Especially the differences for ΔN are substantial. The dephasing index however, which is arguably the more important or useful observable, is not so fluctuant despite it's direct connection to the dephasing.

For the observables other than ΔN the differences rarely seem to become greater than 12%. As mentioned, the code broke down for higher values of m_2 than the used ones, but there is a clear trend towards smaller differences, meaning the newer equations should be less relevant when considering EMRIs instead.

As mentioned in the results, some of the curves look similar but are shifted along the x-axis. For non-constant functions, this automatically results in some difference compared to the unaltered version. Which in this case most likely boosts the differences for a lot of the values. This would also be compatible with the many instances of swaping signs. Analyzing the severity of of the frequency shifts could make for interesting future work. If the shift is

known and the curves indeed are very similar otherwise, simulations could be calculated with the simpler equations and then just shifted in the frequency. It has to be noted however, that it is possible for the similar shape of the curves to appear due to some numerical artifacts that elude direct notice.

References

[1] Nicolaus Copernicus. *On the revolutions of heavenly spheres*. Prometheus Books, 2010.

[2] Alexander Givental. "Kepler's laws and conic sections". In: *Arnold Mathematical Journal* 2 (2016), pp. 139–148.

[3] Albert Einstein et al. "On the electrodynamics of moving bodies". In: *Annalen der physik* 17.10 (1905), pp. 891–921.

[4] Fritz Zwicky. "Die rotverschiebung von extragalaktischen nebeln". In: *Helvetica Physica Acta, Vol. 6, p. 110-127* 6 (1933), pp. 110–127.

[5] Edward Purcell. "Observation of a line in the galactic radio spectrum". In: *Nature* 168 (1951), p. 356.

[6] A Araujo, DF López, and JG Pereira. "De Sitter-Invariant Special Relativity and Galaxy Rotation Curves". In: *Gravitation and Cosmology* 25 (2019), pp. 157–163.

[7] Vera C Rubin and W Kent Ford Jr. "Rotation of the Andromeda nebula from a spectroscopic survey of emission regions". In: *Astrophysical Journal, vol. 159, p. 379* 159 (1970), p. 379.

[8] Mordehai Milgrom. "A modification of the Newtonian dynamics as a possible alternative to the hidden mass hypothesis". In: *Astrophysical Journal, Part 1 (ISSN 0004-637X), vol. 270, July 15, 1983, p. 365-370. Research supported by the US-Israel Binational Science Foundation.* 270 (1983), pp. 365–370.

[9] Hans A Buchdahl. "Non-linear Lagrangians and cosmological theory". In: *Monthly Notices of the Royal Astronomical Society* 150.1 (1970), pp. 1–8.

[10] Risa H Wechsler and Jeremy L Tinker. "The connection between galaxies and their dark matter halos". In: *Annual Review of Astronomy and Astrophysics* 56.1 (2018), pp. 435–487.

[11] Gianfranco Bertone. *Particle dark matter: observations, models and searches*. Cambridge University Press, 2010.

[12] David N Spergel and Paul J Steinhardt. "Observational evidence for self-interacting cold dark matter". In: *Physical review letters* 84.17 (2000), p. 3760.

[13] Oliver D Elbert et al. "Core formation in dwarf haloes with self-interacting dark matter: no fine-tuning necessary". In: *Monthly Notices of the Royal Astronomical Society* 453.1 (2015), pp. 29–37.

[14] BP Abbott et al. "LIGO: the laser interferometer gravitational-wave observatory". In: *Reports on Progress in physics* 72.7 (2009), p. 076901.

[15] Bernard Caron et al. "The virgo interferometer". In: *Classical and Quantum Gravity* 14.6 (1997), p. 1461.

[16] Karsten Danzmann and Albrecht Rüdiger. "LISA technology—concept, status, prospects". In: *Classical and Quantum Gravity* 20.10 (2003), S1.

[17] Benjamin P Abbott et al. "Observation of gravitational waves from a binary black hole merger". In: *Physical review letters* 116.6 (2016), p. 061102.

[18] Albert Einstein. "Die feldgleichungen der gravitation". In: *Sitzungsberichte der Königlich Preußischen Akademie der Wissenschaften* (1915), pp. 844–847.

[19] Albert Einstein. "Kosmologische Betrachtungen zur allgemeinen Relativitätstheorie". In: *Sitzungsberichte der Königlich Preussischen Akademie der Wissenschaften* (1917), pp. 142–152.

[20] P. J. E. Peebles and Bharat Ratra. "The cosmological constant and dark energy". In: *Rev. Mod. Phys.* 75 (2 2003), pp. 559–606. DOI: 10.1103/RevModPhys.75.559. URL: https://link.aps.org/doi/10.1103/RevModPhys.75.559.

[21] Karl Schwarzschild. "Über das Gravitationsfeld eines Massenpunktes nach der einsteinschen Theorie". In: *Sitzungsberichte der königlich preussischen Akademie der Wissenschaften* (1916), pp. 189–196.

[22] Eugeny Babichev, Viatcheslav Mukhanov, and Alexander Vikman. "Escaping from the black hole?" In: *Journal of High Energy Physics* 2006.09 (2006), p. 061.

[23] Roy P Kerr. "Gravitational field of a spinning mass as an example of algebraically special metrics". In: *Physical review letters* 11.5 (1963), p. 237.

[24] Ernesto F Eiroa, Gustavo E Romero, and Diego F Torres. "Reissner-Nordström black hole lensing". In: *Physical Review D* 66.2 (2002), p. 024010.

[25] Tim Adamo and Ezra T Newman. "The Kerr-Newman metric: a review". In: *arXiv preprint arXiv:1410.6626* (2014).

[26] Michele Maggiore. *Gravitational Waves: Volume 1: Theory and Experiments*. Oxford University Press, Oct. 2007. ISBN: 9780198570745. DOI: 10.1093/acprof:oso/9780198570745.001.0001. URL: https://doi.org/10.1093/acprof:oso/9780198570745.001.0001.

[27] James M Bardeen, William H Press, and Saul A Teukolsky. "Rotating black holes: locally nonrotating frames, energy extraction, and scalar synchrotron radiation". In: *Astrophysical Journal, Vol. 178, pp. 347-370 (1972)* 178 (1972), pp. 347–370.

[28] Roger R Bate, Donald D Mueller, and Jerry E White. "Fundamentals of Astrodynamics. 1971". In: *Courier Corporation* ().

[29] Christopher J Moore, Robert H Cole, and Christopher PL Berry. "Gravitational-wave sensitivity curves". In: *Classical and Quantum Gravity* 32.1 (2014), p. 015014.

[30] Yu-Chen Zhou et al. "Intermediate-mass-ratio inspirals with general dynamical friction in dark matter minispikes". In: *arXiv preprint arXiv:2405.19240* (2024).

[31] Niklas Becker and Laura Sagunski. "Comparing accretion disks and dark matter spikes in intermediate mass ratio inspirals". In: *Physical Review D* 107.8 (2023), p. 083003.

[32] Bradley J Kavanagh et al. "Detecting dark matter around black holes with gravitational waves: Effects of dark-matter dynamics on the gravitational waveform". In: *Physical Review D* 102.8 (2020), p. 083006.

[33] Piero Madau and Mark Dickinson. "Cosmic star-formation history". In: *Annual Review of Astronomy and Astrophysics* 52.1 (2014), pp. 415–486.

[34] Adam Coogan et al. "Measuring the dark matter environments of black hole binaries with gravitational waves". In: *Physical Review D* 105.4 (2022), p. 043009.

[35] Paolo Gondolo and Joseph Silk. "Dark matter annihilation at the galactic center". In: *Physical Review Letters* 83.9 (1999), p. 1719.

[36] Julio F Navarro. "The structure of cold dark matter halos". In: *Symposium-international astronomical union*. Vol. 171. Cambridge University Press. 1996, pp. 255–258.

[37] Stuart L Shapiro and Vasileios Paschalidis. "Self-interacting dark matter cusps around massive black holes". In: *Physical Review D* 89.2 (2014), p. 023506.

[38] Ralph Abraham and Jerrold E Marsden. *Foundations of mechanics*. 364. American Mathematical Soc., 2008.

[39] Kazunari Eda et al. "Gravitational waves as a probe of dark matter minispikes". In: *Physical Review D* 91.4 (2015), p. 044045.

[40] Xiao-Jun Yue and Zhoujian Cao. "Dark matter minispike: A significant enhancement of eccentricity for intermediate-mass-ratio inspirals". In: *Physical Review D* 100.4 (2019), p. 043013.

[41] Niklas Becker et al. "Circularization versus eccentrification in intermediate mass ratio inspirals inside dark matter spikes". In: *Physical Review D* 105.6 (2022), p. 063029.

[42] Fani Dosopoulou. "Dynamical friction in dark matter spikes: Corrections to Chandrasekhar's formula". In: *Physical Review D* 110.8 (2024), p. 083027.

Selbstständigkeitserklärung

Hiermit erkläre ich, dass ich die Arbeit selbstständig und ohne Benutzung anderer als der angegebenen Quellen und Hilfsmittel verfasst habe. Alle Stellen der Arbeit, die wörtlich oder sinngemäß aus Veröffentlichungen oder aus anderen fremden Texten entnommen wurden, sind von mir als solche kenntlich gemacht worden. Ferner erkläre ich, dass die Arbeit nicht - auch nicht auszugsweise - für eine andere Prüfung verwendet wurde.

Ort, Datum: _____ Unterschrift: _____